POLITECNICO DI TORINO

Master of Science's Degree in Biomedical Engineering

Politecnico di Torino

1859

Master of Science's Degree Thesis

Analyzing human lower limb kinematics during walking: a challenging study with minimal inertial sensor configuration

Supervisors

Prof. Ing. Andrea CEREATTI

Dott. Ing. Marco CARUSO

Candidate

Samira FRANCESCA

December 2023

Abstract

Wearable technology and sensor fusion techniques have enabled the study of mobility in real-life conditions, with a specific focus on Inertial Measurement Units (IMUs) due to their portability and versatility. A popular and powerful configuration proposed and validated in the literature [1] involves instrumenting the pelvis and feet with IMUs. This setup allows the capture of spatio-temporal parameters and center-of-mass movements but lacks information about joint angles. Consequently, the description of lower limb movements remains incomplete. To obtain a comprehensive understanding of joint angles and reconstruct lower limb kinematics, attaching an IMU to each segment proximal and distal to the joint of interest would be necessary. Joint angles are determined by assessing the relative orientation between distal and proximal segments. However, this full configuration increases experimental complexity, subject preparation times, and costs, making it impractical for real-world scenarios. This thesis aimed to explore the feasibility of obtaining an acceptable description of joint kinematics during in-lab walking using this strategic three-IMU configuration, without escalating experimental complexity. To reconstruct the kinematic chain, in addition to the orientations obtained from the IMUs, we exploited the spatio-temporal parameters to address missing information; however, both are affected by errors. For this reason, an optimization framework had to be implemented to fit these quantities to a biomechanical model of the lower limbs. The biomechanical model was based on the Denavit-Hartenberg convention and incorporated three rotations for each joint. These joints were defined according to the rotation sequences and axis orientations recommended by the International Society of Biomechanics guidelines, which is useful for standardizing results. To limit the errors affecting the IMU-based position and orientation, two set of constraints including limits on joint angles and gait-specific conditions were introduced. The initial set addressed permissible ranges for hip, knee, and ankle angles during walking. The second set delineated the characteristics of the analyzed gait, such as rectilinear motion, ensuring, for instance, that the variation in joint positions was positive in the anteroposterior direction. The Sequential Quadratic Programming algorithm was employed for optimization, which minimizes an objective function that considers the differences between the orientation and position quantities obtained from the model and those obtained from the three IMUs. The experimental validation, conducted in a controlled environment at this stage, compared the proposed IMU-based system with a stereophotogrammetric system (SP), validating its accuracy and feasibility in a straight-line walking condition at comfort speed. Root Mean Square Error (RMSE) values, calculated by comparing joint angles from the proposed method

with those from the SP after mean value removal, were 4.3, 6.1, and 4.8 degrees for hip, knee, and ankle joints, respectively. Generally, joint kinematics estimation systems are deemed acceptable with RMSE errors below 5 degrees [2]. This study highlighted the effectiveness of a minimal IMU configuration in capturing vital kinematic data during walking, presenting solutions for wearable sensor network challenges. Preliminary validation of the developed framework showed a significant step in the incorporation of IMU technology for real-world human movement analysis and its potential in providing more accessible and efficient clinical gait assessments. With further comprehensive validation, including several pathological cases and complex exercises in real-life scenarios, this technology could contribute to improved diagnosis and monitoring of motor disorders.

Table of Contents

List of Tables

List of Figures

Acronyms

DH

Denavit-Hartenberg

DoF

Degree of Freedom

DRI

Direct Reverse Integration

GCS

Global Coordinate System

INDIP

INertial module with DIstance sensors and Pressure insoles

ISB

International Society of Biomechanics

IMU

Inertial Measurement Unit

LCS

Local Coordinate System

MEMS

Micro Electro Mechanical System

QP

Quadratic Programming

RMSE

Root Mean Square Error

ROM

Range Of Movement

SFA

Sensor Fusion Algorithm

SL

Stride Length

SP

Stereophotogrammetry

SQP

Sequential Quadratic Programming

ZUPT

Zero-velocity update

Chapter 1

Introduction

1.1 Clinical relevance and general introduction

In the realm of comprehending human movement, the exploration of quantifying the kinematic intricacies of human gait in real-life scenarios holds immense significance. Such an endeavor has the potential to usher in new perspectives and catalyze a paradigm shift in the diagnostic processes of motor disorders, as well as the design and evaluation of rehabilitation interventions. The ability to capture and analyze the dynamic aspects of human gait in naturalistic settings is crucial for obtaining a holistic understanding of an individual's movement patterns. Notably, it has been demonstrated that walking speed can be regarded as the sixth vital sign, following traditional indicators such as body temperature, heart rate, respiratory rate, blood pressure, and oxygen saturation [3].
Quantitative instrumented gait analysis stands out as a potent tool that can provide clinicians with precise and reliable gait data, offering invaluable insights for both diagnosis and ongoing monitoring of motor disorders. However, the widespread integration of such advanced gait analysis methodologies into clinical practice faces significant challenges primarily related to logistical constraints. The emergence of wearable technology, multi-modal approaches, sensor fusion techniques, and AI-driven computational platforms is rapidly gaining prominence within the realm of gait assessment. These innovative solutions hold the promise of overcoming existing impediments, presenting clinicians with viable alternatives that enable more seamless and efficient gait monitoring in real-world conditions [4]. As we continue to explore and integrate these technological advancements, the potential for enhancing clinical decision-making and optimizing rehabilitation strategies becomes increasingly tangible, marking a transformative era in the field of human movement analysis.
The pursuit of this understanding has led researchers to explore various technological

avenues, among which the use of Inertial Measurement Units (IMUs) stands out as a prominent solution. IMUs, capable of capturing essential kinematic data, offer a direct window into the complexities of human motion. IMUs typically comprises three tri-axial inertial sensors, an accelerometer and a gyroscope, capable of tracking the sensor's orientation within an internal framework. Consequently, these devices, in addition to their compact size, affordability, and low power consumption, can be effectively utilized as wearable devices in real-life situations outside the confines of laboratory settings [5]. When analyzing human walking, IMUs enable the measurement of both kinematic variables and spatio-temporal parameters of gait, although their accuracy is generally lower than that of the optical stereophotogrammetry (SP).

Utilizing signals from the accelerometer and the gyroscope, various digital mobility outcomes can be derived. Specifically, joint angles can be calculated based on the orientation of IMUs attached to the proximal and distal segments of the joint under examination. However, the practical application of full-body sensor networks in real-life scenarios (Figure 1.1.) has proven challenging, often hindered by their bulkiness and inconvenience for individuals engaged in everyday activities [6].
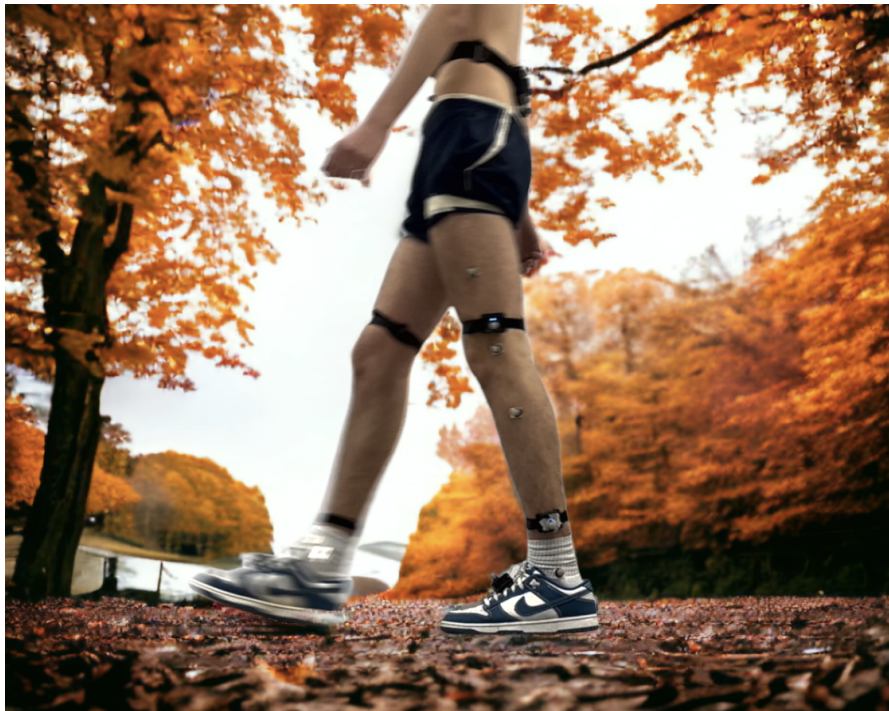
Figure 1.1: Instrumented subject walking in the real world

1.2 Challenge and aim of the thesis

This thesis work was created to solve the problem of having a sensor placed on each body segment to calculate joint angles for real world applications.

As the initial step involves validation, this thesis is primarily centered on the validation process, focusing on the estimation of lower limb kinematics during in-lab walking using a smaller number of IMUs. In fact, by reducing the number of IMUs placed on the subject, a number of advantages are derived, including reduced costs, improved wearability due to a simpler setup, and consequently reduced time for subject pre-treatment. Such advantages become pivotal for extending the study of kinematics outlined in this paper to real-world scenarios.

The choice of the number of sensors to actually use was made by considering a sensor configuration already studied in the literature and accepted by the subjects analysed, namely that consisting of three IMUs placed respectively two on the feet and one on the pelvis [1]. This configuration makes it possible to obtain the spatio-temporal parameters from the IMUs placed on the feet and to define the movements of the centre of mass from the IMU placed on the pelvis. The reason why this thesis is a challenge is that three IMUs alone are not sufficient to derive complete kinematic equations because there is a lack of information. In addition, the parameters estimated by these three IMUs (trajectories and orientations) are affected by errors. Therefore, constraints must be introduced to try to solve this lack of information.

1.3 Thesis outline

The thesis is structured as follows:

In **Chapter 2**, the current advancements in the field are explored, with a specific focus on IMUs, orientation estimation techniques employing Sensor Fusion Algorithms (SFAs), and the estimation of joint kinematics.

In **Chapter 3**, the methods employed in this study are elucidated. This section delves into the interplay between the developed robotic model and the data gathered from IMU sensors, emphasizing the integration of these components within an optimization framework aimed at reconstructing the lower limb kinematics.

In **Chapter 4**, the experimental session is detailed, encompassing an analysis of the experimental protocol and a comprehensive description of the data acquisitions process.

In **Chapter 5**, the results obtained with the implemented optimization framework are displayed.

In **Chapter 6**, the results presented in Chapter 5 are critically discussed.

Chapter 7, summarises the main findings of the thesis and provides an outlook for future research and perspectives.

Chapter 2

State of the art

2.1 Inertial Measurement Units

The increasing adoption of IMUs in gait analysis arises from efforts to overcome significant limitations inherent in optical tracking systems. These constraints include the necessity for specialized laboratories with restricted evaluation spaces, challenges related to marker placement, camera calibration complexities, and the high cost of the required instrumentation [7]. The evolution of IMU sensors became feasible due to advancements in microelectronics, enabling the integration of Micro Electro Mechanical System (MEMS) accelerometers and gyroscopes into a single compact package, as shown in Figure 2.1.
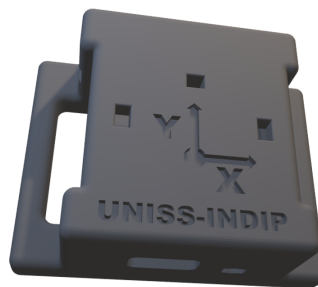
Figure 2.1: Inertial Measurement Unit (INDIP)

IMUs offer several advantages, being highly portable due to their lightweight and compact size, self-powered with low energy consumption, and capable of wireless transmission [8]. Particularly suited for human motion tracking, IMUs eliminate the need for external sources like Infrared LEDs and external sensors such as cameras. Consequently, motion can be recorded outside laboratory settings for extended durations [9]. The fundamental principles underlying IMUs entail minimal intrinsic

latency; any delays primarily stem from wireless data transmission, if applicable, and subsequent processing [9]. This processing can be performed either by an embedded microcontroller onboard or an external processor. Furthermore, IMU sensors are readily available at a low cost, owing to their widespread integration into smartphones and tablet computers, which continue to exhibit enhanced performance [10].

Typically, IMU sensors incorporate orthogonally mounted tri-axis accelerometers and gyroscopes. These sensors are utilized to capture the summation of linear and gravitational accelerations and the angular rate within their Local Coordinate System (LCS) [11]. Through the application of SFAs, a comprehensive estimation of the LCS orientation relative to a Global Coordinate System (GCS) can be achieved by judiciously combining the sensor outputs. As implied by their name, IMUs operate on inertial sensing principles, relying on accelerometers and gyroscopes to estimate attitude (though not heading) concerning the local direction of the gravity vector [12].

2.1.1 Accelerometer

An accelerometer detects the "specific force" ($\mathbf{a}$), which is the vector difference between the body's acceleration ($\mathbf{a}_{body}$) and the gravitational acceleration ($\mathbf{g}$). All quantities are resolved in the LCS of the sensor, and the output is expressed as:

$$\mathbf{a} = (\mathbf{a}_{body} - \mathbf{g}) \tag{2.1}$$

Equation 2.1 indicates that when the device experiences no accelerations, the contribution from $\mathbf{a}_{body}$ is null, and the accelerometer functions as an inclinometer, sensing only the gravitational acceleration. Conversely, during free-fall, the $\mathbf{a}_{body}$ term equals $\mathbf{g}$, rendering the accelerometer output null. In essence, when the IMU is in motion, the $\mathbf{a}_{body}$ term combines with $\mathbf{g}$, making accurate estimation of accelerometer inclination impossible unless additional information sources are utilized. The measured accelerometer output $\mathbf{a}$ is affected by errors, commonly modeled as a matrix of scale factor error coefficients ($\mathbf{S}_a$), a matrix of cross-coupling error coefficients ($\mathbf{M}_a$), a bias error vector ($\mathbf{b}_a$), and its fluctuations vector ($\boldsymbol{\delta}\mathbf{b}_a$), in addition to white Gaussian noise, as stated in equation 2.2 [13, 14]:

$$\mathbf{a} = (\mathbf{S}_a \ \mathbf{M}_a)(\mathbf{a}_{body} - \mathbf{g}) + \mathbf{b}_a + \boldsymbol{\delta}\mathbf{b}_a + \mathbf{w}_a \tag{2.2}$$

In detail, $\mathbf{S}_a$ is a diagonal 3x3 matrix of coefficients representing the deviation of sensor sensitivity from the ideal state for each axis. Typically, this error contains both fixed and temperature-induced variations [15]. $\mathbf{M}_a$ is a 3x3 matrix representing non-orthogonality errors between the three accelerometer sensing axes, caused by mechanical component mounting. Non-orthogonality results in undesired coupling

of axis outputs following a trigonometric formula. The 3x1 vector $\mathbf{b}_a$ represents accelerometer bias, defined as the axis output in the absence of $\mathbf{g}$. $\mathbf{b}_a$ contains both fixed and temperature-induced components. Calibration refinement algorithms can compensate for $\mathbf{S}_a$, $\mathbf{M}_a$, and $\mathbf{b}_a$ errors [16]. However, bias errors also involve run-to-run variations, turn-on to turn-on variations, and gradual changes over time. These components are represented by the 3x1 vector $\boldsymbol{\delta}\mathbf{b}_a$, posing a significant challenge in displacement estimation since the accelerometer output is double integrated after gravitational subtraction. Finally, $\mathbf{w}_a$ is a 3x1 vector of white Gaussian noise with a zero mean. Both $\boldsymbol{\delta}\mathbf{b}_a$ and $\mathbf{w}_a$ vectors fall under stochastic error components and can only be statistically characterized.

2.1.2   Gyroscope

A gyroscope functions by detecting angular velocity along its axes. Various gyroscope output models have been proposed in the literature, differing mainly in the complexity of the slow-varying bias model $\boldsymbol{\delta}\mathbf{b}_g$ [13, 17, 14, 18]. A general model is presented as:

$$\boldsymbol{\omega} = (\mathbf{S}_g \ \mathbf{M}_g) \ \boldsymbol{\omega}_{body} + \mathbf{b}_g + \boldsymbol{\delta}\mathbf{b}_g + \mathbf{w}_g \tag{2.3}$$

It's worth mentioning that other models [16, 13, 14, 18] consider an additional term linking bias dependency on acceleration magnitude due to its effect on the gyroscope MEMS structure. However, this sensitivity to acceleration, as noted by [18], is negligible compared to other error contributions.

In equation 2.3, $\mathbf{S}_g$ and $\mathbf{M}_g$ represent the 3x3 scale factor and non-orthogonality error matrices, respectively. The 3x1 vector $\mathbf{b}_g$ contains the gyroscope bias, defined as the axis output in the absence of rotation. Typically, $\mathbf{b}_g$ is computed during a static acquisition period of a few minutes and then subtracted from gyroscope readings [19]. However, this solution, although simple, may not be entirely effective in practice due to significant changes in the gyroscope bias modeled by $\boldsymbol{\delta}\mathbf{b}_g$. The origin of these fluctuations lies in both mechanical and electronic components, such as changes in drive frequency and voltage generation flicker in digital-analog converters, within a MEMS gyroscope [20, 21, 22]. $\boldsymbol{\delta}\mathbf{b}_g$ constitutes the most influential source of errors in orientation estimation. Integrating angular velocity, including a slow-varying bias, results in orientation drift that grows unbounded over time. This orientation drift directly impacts displacement estimation, as gravity, before subtraction from accelerometer output, must be expressed in the sensor's LCS using the computed orientation. Errors in gravity subtraction lead to significant displacement drift after double integration [10]. Finally, the vector $\mathbf{w}_g$ models white Gaussian noise with a zero mean.

7

2.2 Orientation estimation using a sensor fusion approach

The integration of accelerometer and gyroscope measurements enables the estimation of the three-dimensional orientation of an IMU and, more broadly, the rigid body to which it is affixed. Determining the three-dimensional absolute orientation of an IMU involves defining the rotation between its LCS and the GCS. This step is pivotal for computing joint angles and eliminating the gravitational vector from accelerometer signals, allowing the calculation of linear velocity and displacement. Typically, orientation is estimated using a SFA, also known as a filter, which leverages the strengths and weaknesses of individual sensors within an IMU, as schematized in Figure 2.2.
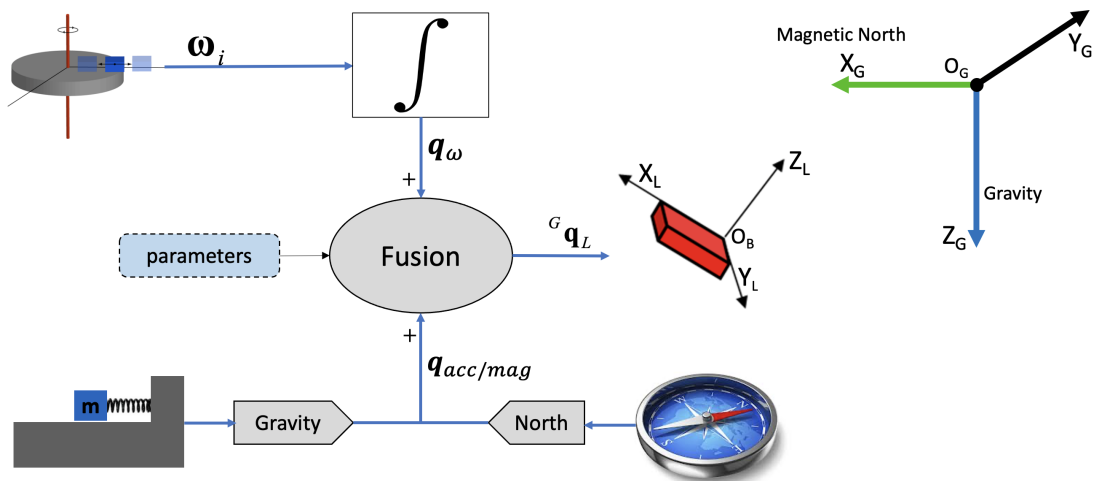
Figure 2.2: Schematization of the operation of a sensor fusion algorithm

Various SFAs have been proposed in the literature, with the majority falling under the complementary or Kalman filtering families. Differences among implementations lie in orientation parametrization (e.g., orientation matrices, quaternions, Euler angles, etc.), diverse formulations of the Kalman filter (e.g., linear, extended, unscented, direct, indirect, etc.), and distinct fusing strategies (optimization or algebraic). A widely employed filter is the one proposed by Madgwick in [23], known as a complementary orientation filter based on quaternions. Noteworthy for its simplicity, this filter necessitates adjustment of only one parameter (β) and imposes a low computational load. The fundamental methodology for determining orientation from IMU data involves integrating angular velocity and subsequently refining this value with accelerometer readings. To delve into specifics, the accelerometer data are utilized in an optimized gradient-descent algorithm, computing

the direction of the gyro measurement error as a derivative of a quaternion. The primary parameter (β) is linked to the zero mean of gyroscope measurement errors, with a higher β assigning more significance to the accelerometer signals.

Numerous studies have attempted to compare the performance of these SFAs over the years, yet conflicting results have been reported, and definitive conclusions regarding IMU orientation accuracy remain elusive [11, 24, 25, 26, 27, 28, 29, 30]. These discrepancies can be attributed to the necessity of appropriately setting the parameters governing the sensor fusion process for each SFA to function effectively. Intrinsic and extrinsic factors, including the magnitude of motion and sensor noise intensity, affect parameter value choices [31]. However, selecting suitable values is non-trivial, and a universally applicable procedure is lacking, rendering result generalization challenging. One possible approach involves identifying optimal values by minimizing the error between estimated and ground truth orientation for specific recordings.

The research [32] validated the pivotal role of selecting suitable parameter values in influencing orientation accuracy levels. It highlighted the need for tailored parameter tuning based on specific experimental conditions [28, 33] to achieve optimal performance. Furthermore, the study revealed that each SFA demonstrates peak performance within a restricted range of parameter values. Changes in experimental conditions may result in significant errors if parameters optimized for a different scenario are used.

2.3   Joint kinematics estimation

The ability to estimate three-dimensional orientation using IMUs has facilitated the tracking of human joint kinematics through wearable sensors [34, 35]. Accurate knowledge of joint angles is crucial in various applications such as sports, ergonomics, clinical evaluations, and telerehabilitation. Each human joint can be viewed as the connection between two adjacent body segments, characterized by a specific number of degrees of freedom (DoFs) based on the joint under analysis. Computation of human joint kinematics necessitates knowledge of the orientation of the two IMUs affixed to the proximal and distal segments of the joint in question. Typically, a IMU's LCS is not aligned with the anatomical coordinate system of the corresponding segments, as defined by the International Society of Biomechanics (ISB) guidelines [36, 37]. After realignment, joint kinematics are defined as distal-to-proximal relative orientation at each time step [38]. Joint angles are obtained through Euler decomposition following the sequence recommended by ISB. This approach is termed unconstrained, as it does not incorporate additional information to mitigate inaccurate orientation errors' effects on joint angles. However, unconstrained joint kinematics offers computational speed and accuracy

advantages under specific experimental conditions such as short durations and absence of vigorous movements.

Consider the general scenario depicted in Figure 2.3, where the anatomical axes of proximal and distal segments are denoted by subscripts "A_p" and "A_d", respectively. Both A_p and A_d definitions adhere to ISB guidelines, relying on major anatomical landmarks and underlying bone orientations [36, 37]. Typically, these axes align along the longitudinal, medio-lateral, and antero-posterior directions. The two segments are connected by a spherical joint allowing three DoFs. Joint kinematics represent the relative orientation between A_d and A_p, expressed in the A_p coordinate system as:

$$^{A_p}\mathbf{q}_{A_d} = \mathbf{q}^*_{A_p} \otimes \mathbf{q}_{A_d} \tag{2.4}$$

Here, $\mathbf{q}_{A_p}$ and $\mathbf{q}_{A_d}$ denote the actual and unknown orientation of proximal and distal anatomical coordinate systems, respectively, expressed in a common GCS. The relative orientation $^{A_p}\mathbf{q}_{A_d}$ is decomposed into corresponding Euler triplets using ISB standards.
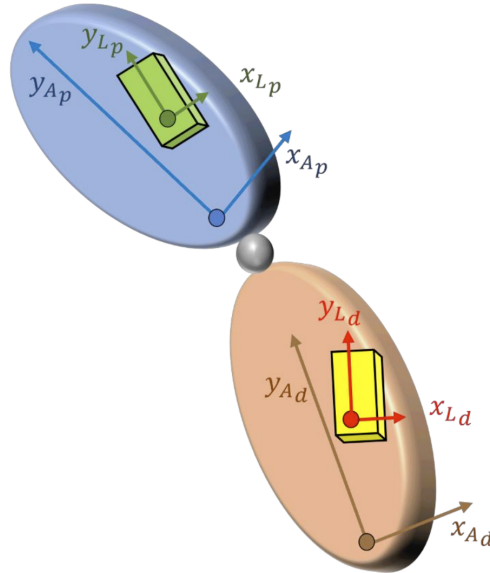
Figure 2.3: Proximal ("p", in blue) and distal ("d", in brown) segments connected by a spherical joint

As shown in Figure 2.3, the primary limitation when estimating joint kinematics with IMUs is the misalignment between each IMU's LCS (technical axes) and the relevant anatomical axes. IMUs are placed on the skin to minimize soft tissue artifacts and avoid movement constraints. Consequently:

$$\mathbf{q}_{A_p} \neq \mathbf{q}_{L_p}, \ \mathbf{q}_{A_d} \neq \mathbf{q}_{L_d} \tag{2.5}$$

Here, $\mathbf{q}_{L_p}$ and $\mathbf{q}_{L_d}$ represent the orientation of proximal and distal IMUs, respectively, as estimated by a SFA. To accurately estimate joint kinematics, understanding the rigid, time-invariant relationship between anatomical and technical axes for each segment is essential, commonly known as "sensor-to-segment alignment". Different methods have been proposed in the literature to address this challenging problem. Among these, manual alignment strikes a balance between simplicity and accuracy.

A second challenge arises when estimating joint kinematics without a magnetometer, lack of information regarding the relative orientation between IMUs on the horizontal plane. The absence of Earth's magnetic field direction precludes the definition of a unique horizontal axis direction in the GCS (designed with the vertical axis aligned to the gravity vector and one horizontal axis aligned with Earth's magnetic field direction projected onto the horizontal plane). Consequently, the SFA cannot estimate the orientation of two IMUs with respect to the same GCS. However, when magnetometer data are omitted, aligning the GCS x-axis with the IMU x-axis is possible. Properly worn IMUs provide a-priori knowledge of the relative orientation between two GCSs in the "zero-joint configuration" when the joint angle is null.

2.4 Proposed approach for joint kinematics estimation

The computation of human joint kinematics, detailed in Section 2.3, necessitates understanding the orientation of two IMUs affixed to the proximal and distal segments of the specific joint. Consequently, to reconstruct lower limb kinematics, which involves deriving angles at the hip, knee, and ankle, seven IMUs placed on the pelvis, thighs, legs, and feet are typically used.

However, the objective of this study was to simplify this sensor setup by employing only three IMUs situated on the pelvis and feet. This streamlined approach offers numerous advantages, including cost-effectiveness, improved wearability due to a simpler setup, and reduced preparation time for subjects. Although this sensor configuration, previously explored in literature and accepted by analyzed subjects, facilitates spatio-temporal parameter extraction and definition of center-of-mass movements, it presents challenges in deriving comprehensive kinematic equations due to data gaps.

To address this, we leveraged spatio-temporal parameters and IMU-derived orientations, albeit affected by errors, to reconstruct the kinematic chain. Consequently, an optimization framework had to be implemented to fit these quantities to a biomechanical model of the lower limbs.

Chapter 3

Methods

3.1 General description of the analyzed situation

Figure 3.1 illustrates a sagittal view that depicts the scenario under analysis. Specifically, the estimation of lower limb kinematics involves deriving angles at the hip, knee, and ankle joints, designated as φ_1, φ_4, and φ_7, respectively. This is accomplished by leveraging the position and orientation information of the feet and pelvis, without possessing knee-specific information. The available data is incorporated into an optimization framework, aiming to reconstruct lower limb kinematics while adhering to established relationships among the three angles at the hip, knee, and ankle, connected by segments of known length.

The discussion presented for the sagittal plane is further expanded to encompass other planes, allowing the derivation of not only flexion-extension angles but also adduction-abduction and intra-extra rotation angles.

3.2 Overview of the optimization framework

To reconstruct the kinematics of lower limbs during walking, an optimization framework, illustrated in Figure 3.2, was employed to derive joint angles and positions. This framework, implemented in MATLAB, comprises a central optimization block that takes input from two sources: the lower limb model and data obtained from IMUs. It then outputs joint angles and positions, allowing the reconstruction of joint kinematics for each analyzed moment.

As mentioned in Chapter 1, compensating for the limited information from IMUs necessitated the introduction of constraints. These constraints were applied in the first of the aforementioned input blocks, specifically in relation to the lower limb model. To provide a clearer understanding of these constraints, they can be categorized into two types: constraints on joints, which pertain to functional
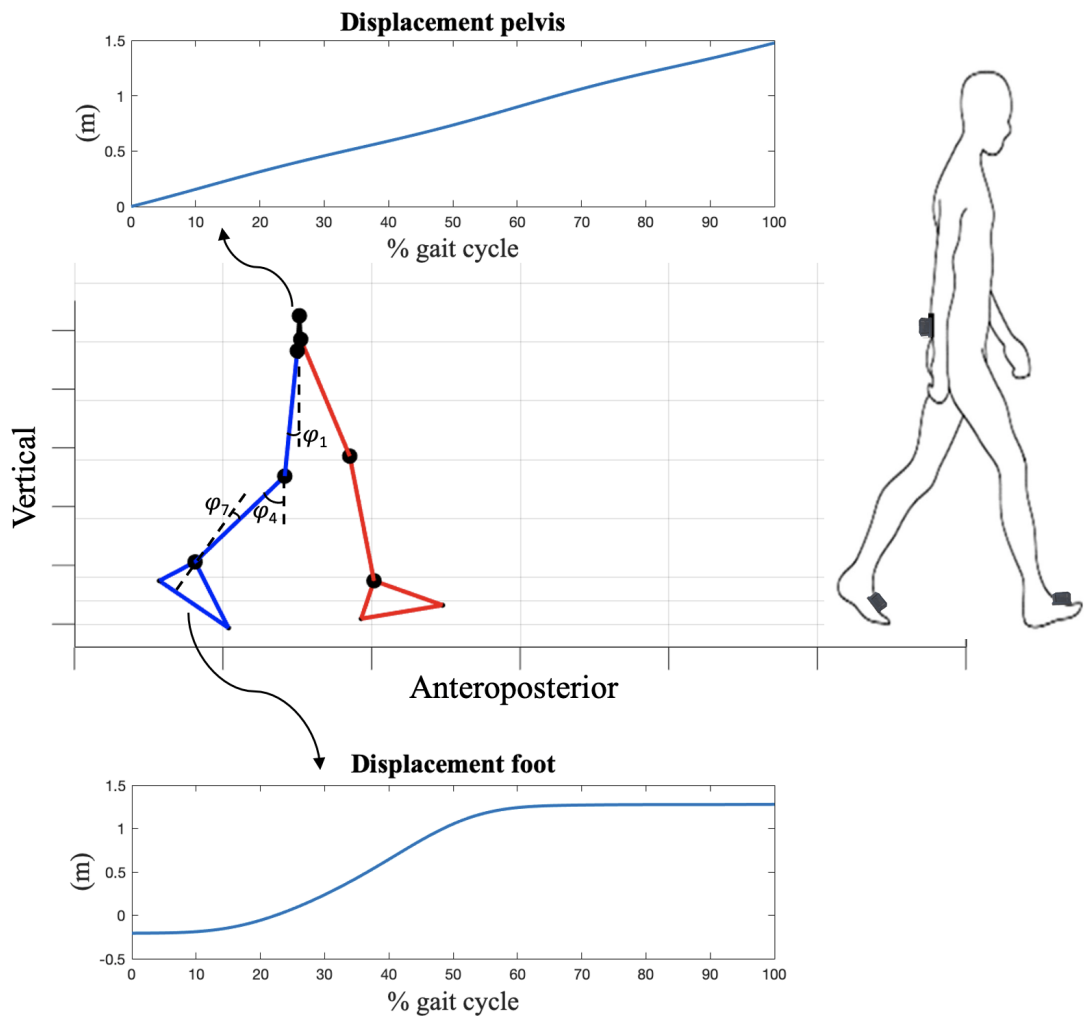
Figure 3.1: Sagittal view of the diagram representing the situation under analysis
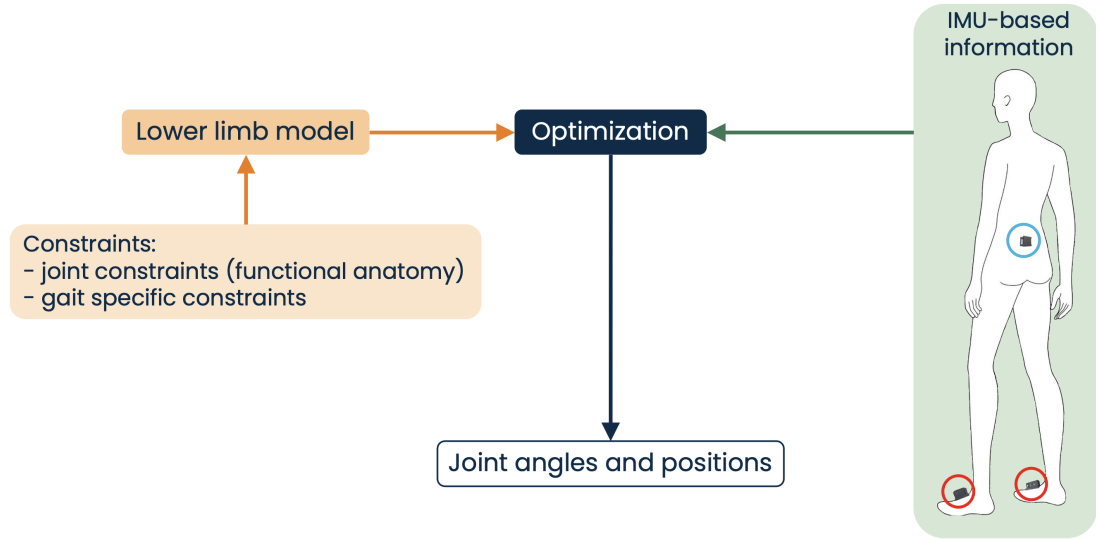
Figure 3.2: Overview of the optimization framework

anatomy, and constraints specific to the analyzed experiment, such as gait patterns. A more detailed explanation of these constraints is provided in Section 3.4.

3.3   Lower limb model

3.3.1   The Denavit-Hartenberg convention

The initial input block for optimization involved the lower limb model, which was structured as a chain following the Denavit-Hartenberg (DH) convention commonly used in robotics [39]. A representation of this modeling based on the DH convention is depicted in Figure 3.3.

In this convention, the pose matrix A_i^{i-1}, encompassing both orientation and position, of the ith link in relation to the pose of the $i - 1^{th}$ link, is defined using four parameters (a_i, d_i, α_i and θ_i). These parameters are defined as follows:

- a_i distance between O_i and $O_{i'}$,

- d_i coordinate of $O_{i'}$ along z_{i-1},

- α_i angle between axes z_{i-1} and z_i about axis x_i to be taken positive when rotation is made counter-clockwise,

- θ_i angle between axes x_{i-1} and x_i about axis z_{i-1} to be taken positive when rotation is made counter-clockwise.
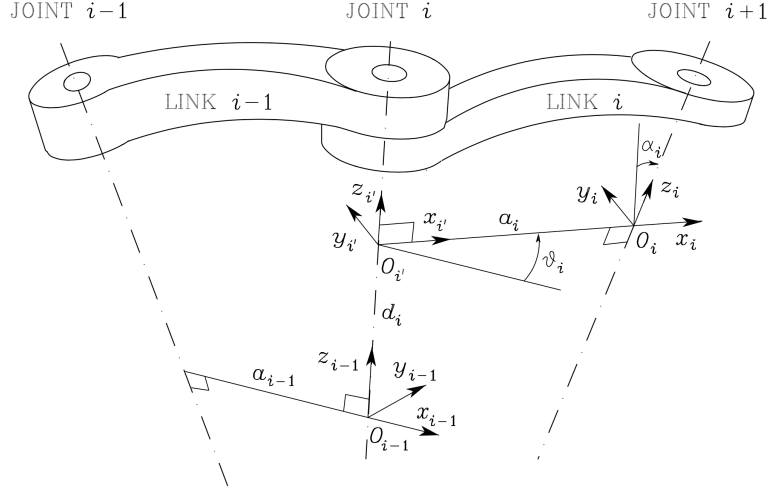
Figure 3.3: Denavit-Hartenberg convention [39]

According to the DH convention, each joint is modeled with a single DoF whose rotation is quantified with φ. If the ith joint is revolute, three of the four parameters (a_i, d_i and α_i) are constant and depend only on the geometry of connection between consecutive joints established by the ith link. Only the remaining variable θ_i is variable over time.

The DH convention defines the transformation matrix of the ith link with respect to $i - 1^{th}$ link, as follows:

$$
A_i^{i-1} = \begin{bmatrix} \cos(\theta) & -\sin(\theta)\cos(\alpha) & \sin(\theta)\sin(\alpha) & a\cos(\theta) \\ \sin(\theta) & \cos(\theta)\cos(\alpha) & -\cos(\theta)\sin(\alpha) & a\sin(\theta) \\ 0 & \sin(\alpha) & \cos(\alpha) & d \\ 0 & 0 & 0 & 1 \end{bmatrix} \tag{3.1}
$$

3.3.2 The developed lower limb model

The DH convention has found widespread application in various studies within the literature. For instance, in Panich's research [40], the convention was employed to model leg-exoskeleton, enabling the representation of three DoFs for each leg joint: hip, knee, and ankle. Another notable application of the DH convention can be seen in Chen's study [41], where it was utilized for IMU-based lower limb motion trajectory estimation. In this research, five IMU sensors positioned on the pelvis, thighs, and legs were employed.

In this thesis work, the DH convention was adopted to model the human lower limbs as a chain of rigid links, taking into account the anthropometric lengths of each segment (l_{THIGH}, l_{SHANK}, $l_{TOE-ANKLE}$, l_{FOOT}). The model incorporated three

revolute joints for the pelvis and nine revolute joints for each lower limb. These joints were defined based on rotation sequences and axis orientations recommended by the ISB guidelines [36]. The individual joints, including pelvis, hip, knee, and ankle, were endowed with three DoFs each, encompassing flexion-extension, adduction-abduction and intra-extra-rotation [42], as depicted in Figure 3.4. As all joints in the model were revolute, the variable value θ_i was the only parameter dependent on φ_i. The corresponding DH parameters were established as outlined in Table 3.1 and in Table 3.2.

Link	θ_i	d_i	ai	α_i
1	$\varphi_1+\pi/2$	0	0	$\pi/2$
2	$\varphi_2+\pi/2$	0	0	$\pi/2$
3	$\varphi_3+\pi/2$	0	0	$\pi/2$

Table 3.1: Denavit-Hartenberg parameters for the pelvis

Link	θ_i	d_i	ai	α_i
1	$\varphi_1+\pi/2$	0	0	$\pi/2$
2	$\varphi_2+\pi/2$	0	0	$\pi/2$
3	$\varphi_3+\pi/2$	$-l_{THIGH}$	0	$\pi/2$
4	$\varphi_4+\pi/2$	0	0	$\pi/2$
5	$\varphi_5+\pi/2$	0	0	$\pi/2$
6	$\varphi_6+\pi/2$	$-l_{SHANK}$	0	$\pi/2$
7	$\varphi_7+\pi/2$	0	0	$\pi/2$
8	$\varphi_8+\pi/2$	0	0	$\pi/2$
9	$\varphi_9+\pi/2$	$-h_{FOOT}$	$l_{TOE-ANKLE}$	0
10	0	0	$-l_{FOOT}$	0

Table 3.2: Denavit-Hartenberg parameters for lower limbs

The constructed model enabled the initiation of the analysis from specific angle configurations for each joint. Utilizing direct kinematics, the model yielded essential information, including the orientation and position of the pelvis, right foot, and left foot. These parameters served as one of the two inputs for the optimization process, as illustrated in Figure 3.6.
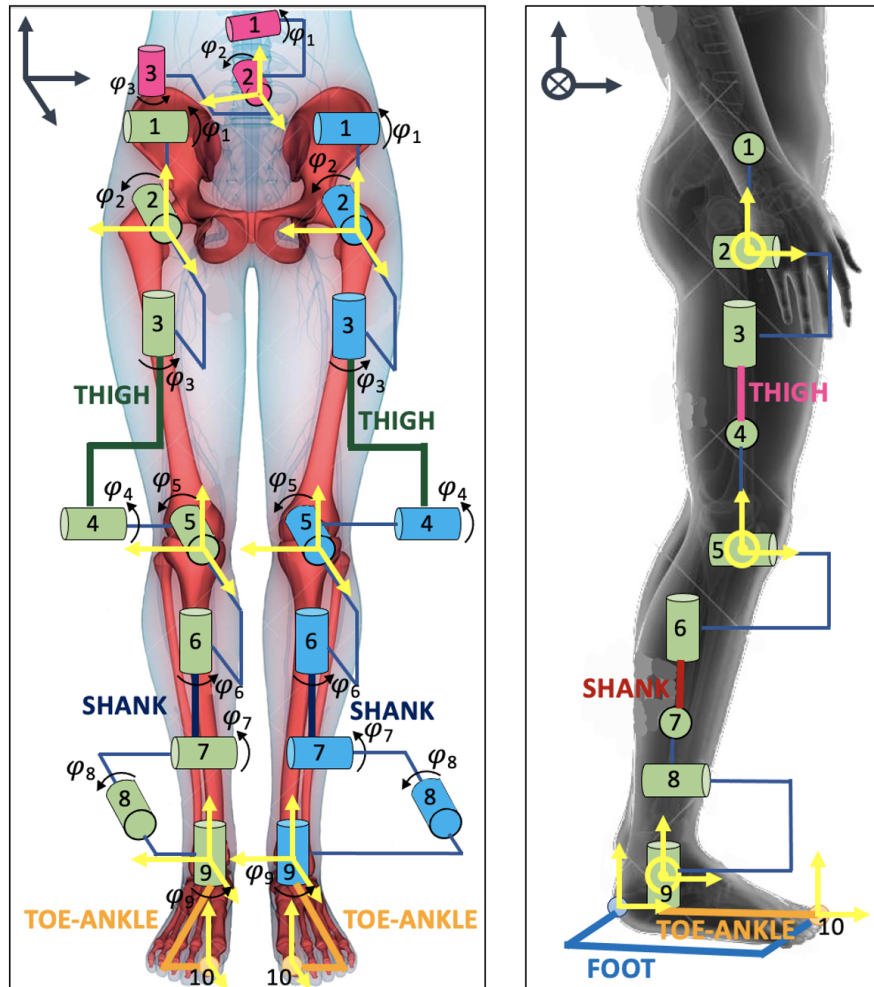
Figure 3.4: Frontal and sagittal view of the human lower limbs model in agreement with DH and with the ISB guidelines. The joints are numbered from 1 to 3 for the pelvis and from 1 to 9 for each lower limb. Links represented with thin blue line are characterized by a null length.

3.4 Constraints

The previously outlined lower limb model facilitated the introduction of constraints to compensate for the limited information gathered from the IMUs. As noted earlier, these constraints can be categorized into two groups:

1. **Constraints on joints**: These constraints pertain to the functional anatomy and were applied to the rotations of each joint. Specifically, the flexion-extension angles of the joints in both lower limbs were restricted, as detailed in Table 3.3, to prevent unrealistic rotations during walking [43]. Additionally, the angles of adduction-abduction and intra-extra rotation were either constrained to small values or completely blocked to ensure accuracy.

Angles (deg)	Flexion	Extension
Hip	50	-50
Knee	80	-2
Ankle	50	-10

Table 3.3: Limits imposed on the flexion-extension angles of the lower limb joints

2. **Constraints specific to the analyzed experiment (gait)**: These constraints were designed to align with the particulars of the gait being studied and were crucial in refining the model's accuracy and relevance to real-world walking scenarios. They can be summarised as follows (Figure 3.5):

   (a) No "ghost foot": feet are not allowed to overstep the ground while walking,

   (b) At least one foot in contact with the ground: necessary condition to define walking and distinguish it from running for example,

   (c) Positive position variation in the anteroposterior direction: to prevent the subject from walking backwards,

   (d) Pelvis trajectory within feet in the anteroposterior direction: to avoid forward or backward centre of mass imbalances.

3.5 IMU-based information

The second input block for optimization comprised data obtained from IMUs. Following the setup outlined in [1], IMUs were strategically placed on the pelvis and feet. These sensors provided the same parameters as those derived from the
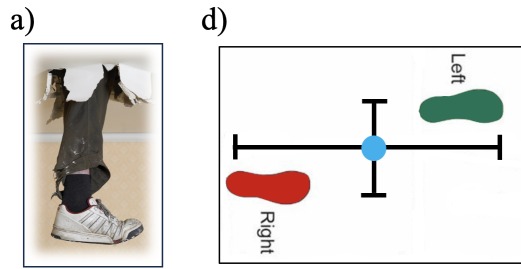
Figure 3.5: a) "No ghost foot"; d) Pelvis trajectory (in light blue) within feet in the anteroposterior direction
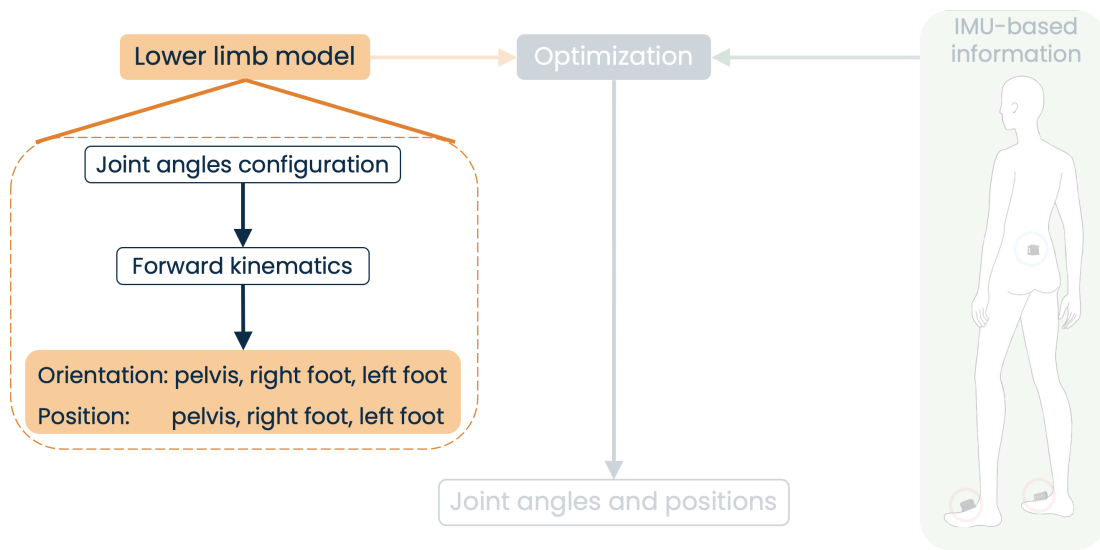
Figure 3.6: Overview of the optimization framework with the quantities derived from the lower limb model made explicit

previously discussed lower limb model, namely the orientation and position of the pelvis, right foot, and left foot. The obtained parameters served as the second input for the optimization process, as illustrated in Figure 3.7, and were instrumental in refining the accuracy and reliability of the optimization framework.

3.5.1 Orientation estimation

The orientation of the pelvis and feet was determined using the method proposed by Madgwick in [23]. The Madgwick filter is a complementary quaternion-based orientation filter and it was selected for its simplicity, requiring the adjustment of only one parameter (β) and exhibiting a low computational load. The fundamental
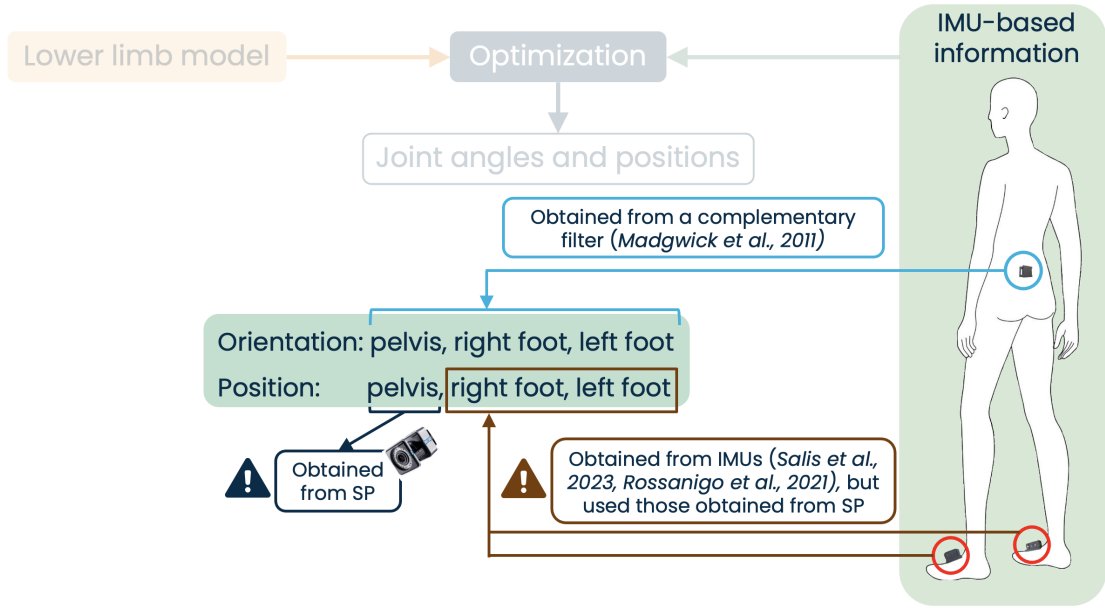
Figure 3.7: Overview of the optimization framework with the quantities derived from the IMUs made explicit

approach to determining orientation from IMU data involves integrating the angular velocity and subsequently correcting this value with accelerometer readings. To be more specific, accelerometer data are employed in an optimized gradient-descent algorithm to compute the direction of the gyroscope measurement error as a quaternion derivative. The primary parameter (β) is associated with the zero mean of gyroscope measurement errors. Essentially, a higher β places greater emphasis on the accelerometer signals. For this study, the chosen value for β was established at 0.001. The algorithm discussed operates in a repetitive cycle where, at each time step, a new orientation is computed based on the previous step. Consequently, the selection of the initial quaternion is crucial for initiating this cycle. A reasonable assumption is made that initially, the body segment to which the IMU is attached is stationary before any motion occurs. This assumption guides the choice of a quaternion initialization method that doesn't necessitate the consideration of gyroscope data, as explained in [44]. Orientation was derived using both accelerometer and gyroscope data. To ensure accuracy, the offset from the gyroscope data was reduced, and this offset was computed as the average of angular velocity values recorded during static conditions, specifically, during the warm-up phase of the sensors. In addition, orientation was recalculated at the initiation of each stride cycle. Given the cyclic nature of walking, particularly during the stance phases where the velocity of the foot nullifies, these instances were opportunistically utilized for reinitialization. Figure 3.8 provides a schematic

representation of the described concept.

3.5.2   Estimation of spatio-temporal gait parameters

The position of the feet was calculated using the spatial parameter estimation method detailed in [45]. The algorithm, which outlines the estimation of stride length (SL), comprises the following sequential steps [46, 47, 48]:

1. Identification of gait events: Initial and final ground contacts are estimated using methods proposed by Salarian et al. [49] and Trojaniello et al. [50], adapted for foot positioning.

2. Identification of integration intervals: SL estimation relies on double integration over time of acceleration components, and integration drift is mitigated by assuming zero-velocity at each integrating instant [51]. The beginning and end of the stride cycle are pinpointed during mid-stance in the flat-foot phase. A zero-velocity update (ZUPT) detector, employing the gyroscope signal, determines the flat-foot phase [47]. The detector assesses the stationary or moving state of the IMU by comparing a function of angular velocity with a threshold *th*. The zero-velocity hypothesis holds if the function is lower than *th*:

$$\frac{\sum_j \|\omega_j\|^2}{N} \leq th \tag{3.2}$$

   where $\|\omega_j\|$ is the norm of angular velocity at the j-th instant, *N* is the window size, and *th* is the threshold value. The ZUPT threshold *th* is set equal to 0.27.

3. Orientation estimation and gravity subtraction: To subtract gravity from raw accelerations, 3D foot orientation is required. A complementary filter, based on the sensor fusion algorithm proposed by Madgwick [23], is employed for this purpose. This filter enables the tuning of a single parameter (β), set equal to 0.001. Additionally, to eliminate gravity residuals, the mean acceleration is subtracted, given that when a body initiates and concludes its motion, the average acceleration must be zero.

4. Re-orientation along the direction of progression: Since SL is defined as anteroposterior displacement during a gait cycle, the coordinate system at each stride is rotated from the sensor system to the anatomical (anteroposterior-mediolateral-vertical) system. The angle maximizing the mean anteroposterior linear velocity for each stride is chosen to identify the direction of progression, and the filtered acceleration is projected onto it [48].

21

5. Direct and reverse integration: Once stride direction and the integration interval are determined, a double integration of gravity-free linear accelerations is performed. To reduce integration drift due to noise and residual gravity, the velocity is estimated using the direct and reverse integration method (DRI) [48]. The DRI involves weighting direct and reverse integrations over time with respect to a sigmoid-shaped weighting function w(t), normalized between 0 and 1, where L is the length of the integration interval, and γ establishes the curve steepness.

$$w(t) = \arctan\left(\frac{2t - L}{2\gamma L}\right) \tag{3.3}$$

6. Displacement estimation: SL is obtained by integrating velocity between two consecutive mid-stance instants.

However, for the current phase of the study, the foot position derived from the SP was employed. Furthermore, the position of the pelvis was also determined using the SP.
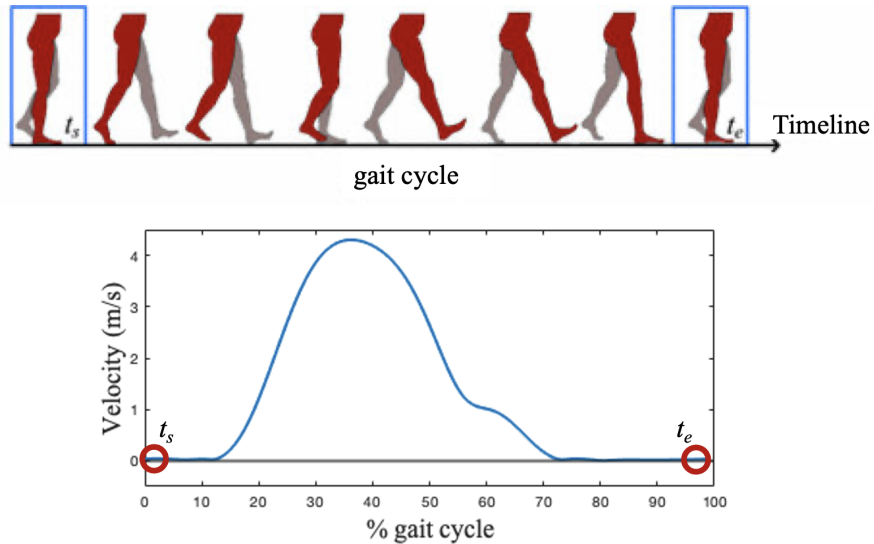
Figure 3.8: Velocity of the center of the foot during gait phases [52]

22

3.6 Definition of the objective function for optimization

3.6.1 The Sequential Quadratic Programming algorythm

The two aforementioned inputs were incorporated into the optimization process, which is elaborated upon in this section.

The applied optimization technique is based on the Sequential Quadratic Programming (SQP) algorythm, an iterative method designed for constrained nonlinear optimization. SQP can be regarded as a quasi-Newton method and is particularly suitable for mathematical problems characterized by twice continuously differentiable objective functions and constraints. SQP methods work by solving a series of optimization subproblems, each of which optimizes a quadratic model of the objective function while linearizing the constraints. The formulation of a quadratic programming (QP) subproblem is based on a quadratic approximation of the Lagrangian function, and its solution is used to form a new iteration, as summarized in Figure 3.9. Consider a nonlinear programming problem of the form:

$$min_x \ f(x)$$
$$\text{subject to } h(x) \geq 0, \ g(x) = 0$$

The Lagrangian for this problem is:

$$\mathcal{L}(x, \lambda, \sigma) = f(x) - \lambda h(x) - \sigma g(x) \tag{3.4}$$

where λ and σ are Lagrange multipliers. To find the solution $\nabla\mathcal{L}(x, \lambda, \sigma) = 0$, the SQP algorithm defines an appropriate search direction d_k at an iterate $(x_k, \lambda_k, \sigma_k)$, as a solution of the QP subproblem. In cases without constraints, the method simplifies to Newton's method, aiming to locate a point where the objective gradient becomes zero [53].

The implementation of SQP consists of the following steps [54]:

1. Updating the Hessian matrix

2. Quadratic programming solution

3. Initialization

4. Line search and merit function

Hence, the SQP algorithm necessitates initial conditions and an objective function for minimization.

The SQP algorithm shares similarities with the active-set algorithm, with notable distinctions including:

23
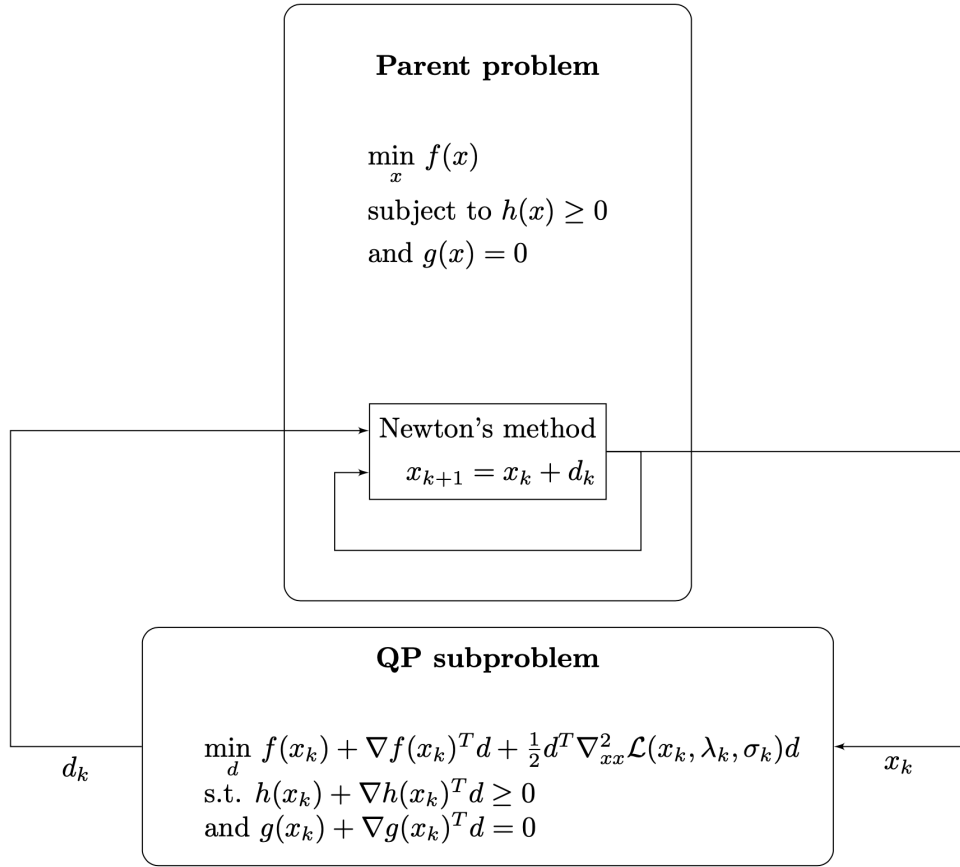
Figure 3.9: General scheme illustrating the basic SQP algorithm [53]. The therms f(x), h(x), and g(x) are each potentially non linear; x is potentially a vector of many variables for the optimization, in which case h(x) and g(x) are systems. ∇^2_{xx} denotes the Hessian matrix.

- Strict feasibility with respect to bounds: The SQP algorithm ensures that each iterative step remains within the bounds-constrained region. Additionally, finite difference steps adhere to these bounds, allowing steps to precisely align with a boundary. This strict feasibility proves advantageous when dealing with undefined or complex objective functions or nonlinear constraint functions outside the bounds-constrained region.

- Robustness to non-double results: Throughout its iterations, the SQP algorithm can encounter failed steps, indicated by an objective function or nonlinear constraint function returning Inf, NaN, or a complex value. In such instances, the algorithm attempts a smaller step.

- Refactored linear algebra routines: The SQP algorithm employs a distinct set of linear algebra routines to solve the quadratic programming subproblem. These routines excel in both memory usage and speed compared to the active-set routines.

- Reformulated feasibility routines: The SQP algorithm introduces two novel approaches to addressing the subproblem when constraints are unsatisfied:

  - The SQP algorithm combines the objective and constraint functions into a merit function, seeking to minimize it under relaxed constraints. While this modified problem may yield a feasible solution, it increases the variable count compared to the original problem, potentially slowing the subproblem solution. These routines draw inspiration from the works [55, 56]. The SQP algorithm adjusts the penalty parameter for the merit function based on the recommendation in [57].

  - In cases where nonlinear constraints are not met, and an attempted step exacerbates the constraint violation, the SQP algorithm endeavors to achieve feasibility using a second-order approximation to the constraints. While this technique may lead to a feasible solution, it can prolong the solution process by necessitating additional evaluations of nonlinear constraint functions.

3.6.2 The objective function

The objective function comprises six terms, outlined in Figure 3.10. To elaborate, the orientation terms were computed by multiplying the model rotation matrix with the transpose of the measured rotation matrix, and the result was converted to Euler angles. Conversely, the position terms were determined as the difference between the model's position and the measured position.

$$f_{obj} = \left[R_{\Delta\_pelvis}, R_{\Delta\_right\_foot}, R_{\Delta\_left\_foot}, p_{\Delta\_pelvis}, p_{\Delta\_right\_foot}, p_{\Delta\_left\_foot} \right]$$

$$R_{\Delta\_pelvis} = R_{pelvis} * (\hat{R}_{pelvis})^T \qquad p_{\Delta\_pelvis} = p_{pelvis} - \hat{p}_{pelvis}$$

model
measure

Euler angles

$$[\alpha_{pelvis}, \beta_{pelvis}, \gamma_{pelvis}]$$
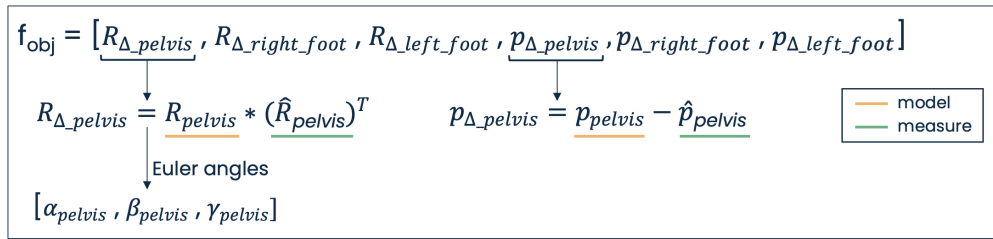
Figure 3.10: Objective function for the Sequential Quadratic Programming algorythm

The summarized optimization process is illustrated in Figure 3.11. Upon completion of the optimization, the output included the angles and positions of the

analyzed joints. This outcome enabled the reconstruction of lower limb kinematics during the studied gait.
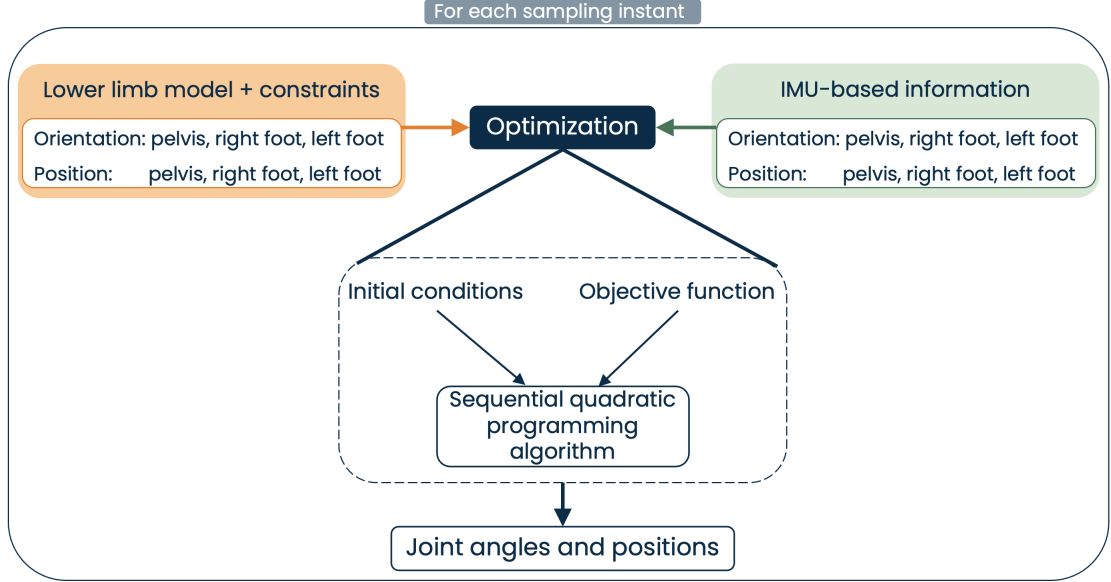
Figure 3.11: Overview of the optimization framework with the optimization process made explicit

3.7 Joint angles and positions

The optimization framework outlined in Section 3.6 was applied to three specific segments of the captured gait data, each corresponding to a single stride. Through this process, the framework generated joint angles and positions crucial for reconstructing the lower limb kinematics. These angles were instrumental in reconstructing the lower limb kinematics. The obtained results were compared with those acquired from the SP to assess the accuracy of the estimation. To facilitate a quantitative comparison between the outcomes derived from the IMUs and those acquired from the SP, Root Mean Square Error (RMSE) values were computed, indicating the differences between the results obtained through the two methods, after removing their mean values. The RMSE calculation formula employed is as follows:

$$RMSE = RMS(\alpha_{SP} - mean(\alpha_{SP}) - (\alpha_{IMU} - mean(\alpha_{IMU})) \qquad (3.5)$$

The terms α_{SP} and α_{IMU} represent the time-series data of angles obtained from the SP and IMU systems, respectively. Removal of the mean value was necessary due

to differing definitions of the anatomical reference system between the two systems, as detailed in [58]. This discrepancy resulted in an offset shift between α_{SP} and α_{IMU}, rendering direct comparison between them meaningless for the purpose of analysis.

Furthermore, Range of Movement (ROM) values were computed for both the angles derived from the IMUs and the SP. Differences between the measurements obtained from the two methods were also taken into account.

Chapter 4

Experimental session

4.1 Experimental setup

In this study, experiments were conducted in the PolitoBIOMed Lab, a facility equipped with specialized instrumentation for movement analysis tests, as shown in Figure 4.1.
Two primary systems were employed:

- SP system as the reference, consisting of:

    - 12 Vicon infrared cameras were used to reduce artefacts caused by natural light, ensuring accurate tracking,

    - 3 RGB cameras recorded video footage of the experiments,

    - An active wand aided in system calibration, featuring known geometric marker configurations, represented in Figure 4.2,

    - 26 passive markers, coated with retroreflective material, were placed on the subjects according to the Vicon's reference guide [59], as shown in Figure 4.3 and in Figure 4.4,

    - A force plate system (Advanced Mechanical Technology, Inc Watertown, USA) facilitated synchronization between the two systems, depicted in Figure 4.2,

    - Nexus software (v. 2.12) was utilized for extracting files containing joint angles and forces.

- IMU-based system: seven IMUs were attached to bands on specific body segments (feet, shanks, thighs, and pelvis) for motion tracking.

Figure 4.1: PolitoBIOMed Lab

Figure 4.2: The force plate system and the active wand

Figure 4.3: Front view of marker placement on the subject [59]
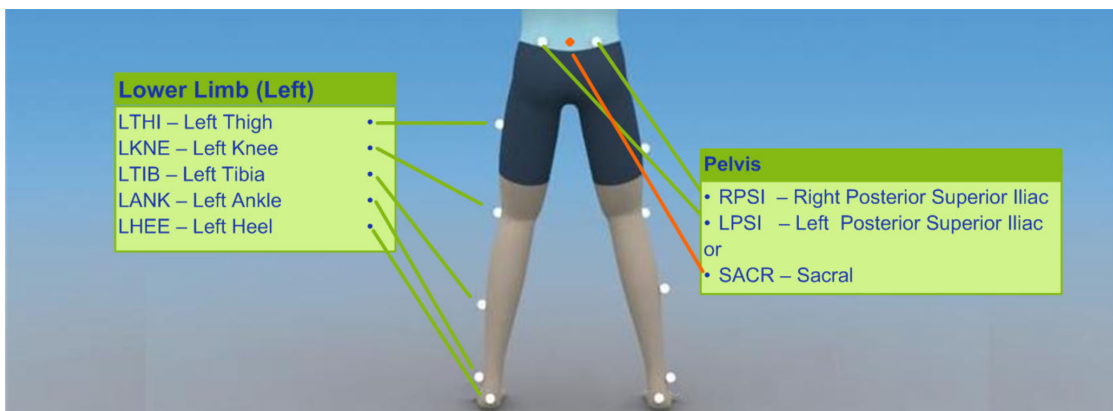
Figure 4.4: Rear view of marker placement on the subject [59]

4.1.1 The INDIP system

The INDIP system (INertial module with DIstance sensors and Pressure insoles) was developed by the University of Sassari with the primary objective of establishing a real-world gold standard for gait analysis [60]. It was strategically incorporated into the European project Mobilise-d, which focuses on generating digital mobility outcomes to monitor the daily gait of individuals with diverse mobility issues, ultimately aiming to enhance personalized care.
The system configuration employed in this project integrates three IMUs affixed to both feet and the lower back, operating at a sampling frequency of 100 Hz.
Each IMU within the system encompasses:

- A 3D accelerometer with a selectable full-scale range of up to ± 16 g, output data rate ranging from 1.6 to 6664 Hz, and low zero-g offset (± 40 mg) [61].

- A 3D gyroscope with a selectable full-scale range of up to ± 2000 °/s, output

data rate ranging from 1.6 to 6664 Hz, and low zero-rate offset (± 1 °/s) [61].

These IMUs are integrated into a printed circuit board, connecting the sensors to transmission modules, the battery, and electronic circuitry for front-ending and data storage. The circuit board is encased in a 3D-printed plastic housing for protection [62].

Two distinct choices for attaching the INDIP units to the subject are available, as shown in Figure 4.5:

- Clips: exclusive for securing to the feet

- Velcro straps: suitable for attachment to the head, hands, lower back, ankles, and feet
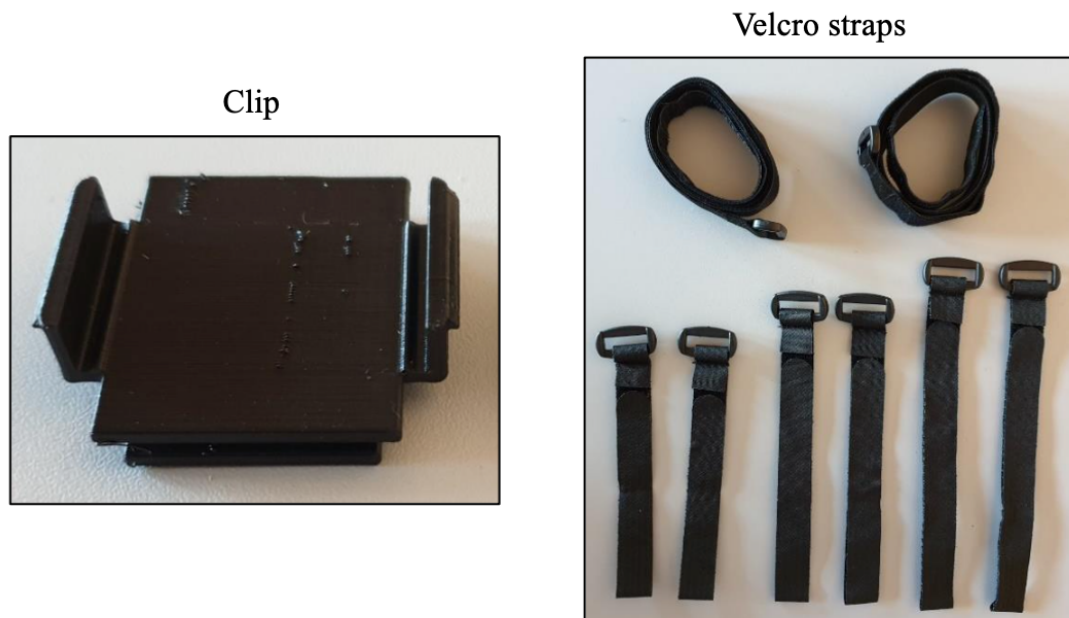
Figure 4.5: Clips and velcro straps for securing the INDIP units

4.1.2 The synchronization process

The synchronization process involves aligning data from different devices with distinct time vectors. Initially, all data are imported, each associated with its unique time vector corresponding to the respective device.

The first synchronization step focuses on aligning the INDIP. Each INDIP dataset is individually interpolated by mapping its original time vector onto the time vector

of an additional INDIP Trigger unit used as a reference. While all INDIP share the same time vector due to their initialization from the same laptop, the starting signals processed via Bluetooth for each INDIP result in varying sample counts for the same trials. To address this, one of the INDIP is chosen as a reference, with the additional INDIP Trigger being the preferred choice due to its synchronization with the SP system. Consequently, the signals from each INDIP are mapped onto the time vector provided by the additional INDIP Trigger, ensuring an equal number of samples for all INDIP.

In the second synchronization step, SP data are aligned with INDIP data by interpolating the optical time vector onto that of the additional INDIP Trigger. This phase is schematized in Figure 4.6. As previously mentioned, both the SP and INDIP Trigger systems start simultaneously through a trigger signal sent via cable. Finally, in the third step, all data are resampled at a constant frequency of 100 Hz. The data from the additional INDIP Trigger are no longer required in the subsequent analysis.
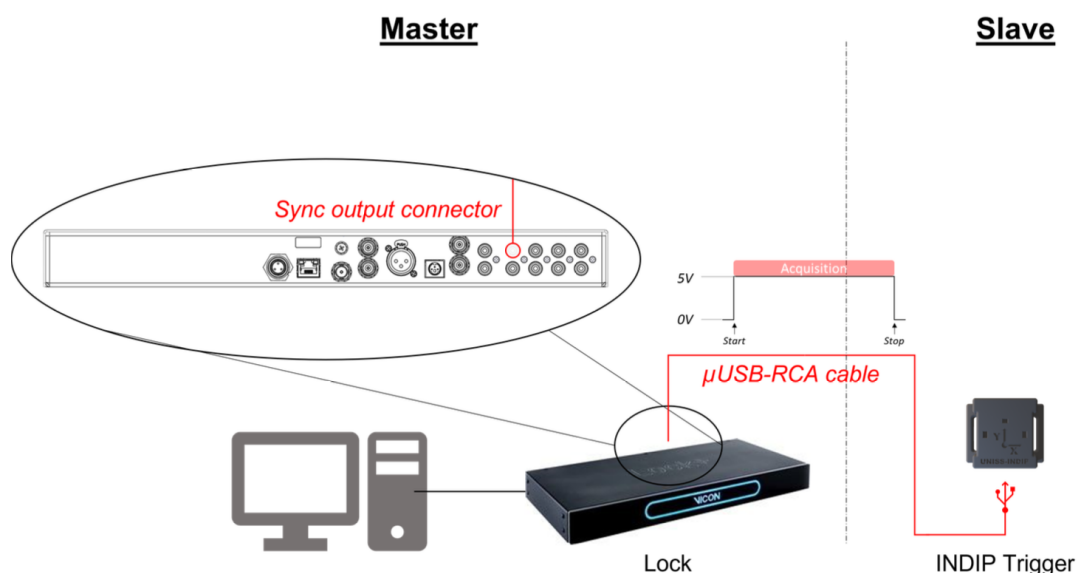
Figure 4.6: Connection between INDIP and Vicon

4.1.3 The calibration process

The sensors embedded in each IMU come pre-calibrated by the integrated circuit manufacturer. However, the initial calibration provided may not be universally suitable for all applications, and its efficacy can diminish over time with usage. Consequently, it is prudent to conduct a thorough examination and, if necessary,

fine-tune the calibration of each sensor to enhance measurement accuracy. Potential calibration parameters include:

- Scale factor (S): These coefficients, which are temperature-dependent, act multiplicatively and are positioned along the diagonal.

- Bias (b): Temperature-dependent biases.

- Cross-axis sensitivity (C): Represented as a matrix, it indicates that perturbing one axis may yield readings on the other two.

- Sensor misalignment (M): Indicates that the three axes may not be perfectly orthogonal, resulting in non-zero acceleration projections on the axes.

- Case-sensor misalignments (optional): Given that the circuit board is housed within a case, uncertainties arise regarding whether the planes identified by the sensors align precisely with those of the case.

Therefore, the complete calibration model for a generic 3D accelerometer is as follows:

$$a_{cal} = MCS(T)[a_{uncal} - b(T)] \tag{4.1}$$

where

- a_{cal} is the calibrated acceleration,

- a_{uncal} represents the uncalibrated acceleration,

- S denotes the scale factor matrix,

- b is the bias,

- C represents the cross sensitivity matrix,

- M denoted the misalignment matrix.

The calibration model outlined is applicable to both the accelerometer and the gyroscope. Specifically, we adopt the calibration methodology proposed by Stancin and Tomazic [63].

Accelerometer calibration

For the accelerometer, the dedicated model is expressed as follows:

$$a = C_s(a_s - a_0) \tag{4.2}$$

where

- a represents the vector of measurements post calibration refinement,

- a_s is the vector of measurements as initially recorded by the accelerometer,

- a_0 signifies the vector of offsets,

- C_s denotes the matrix of scaling coefficients, amalgamating the impact of matrices M, C and S.

Note that, for simplicity, the influence of temperature is not considered.

The primary objective of calibration is to estimate C_s and a_0. We define six distinct acquisitions organized into two sets of triplets, as illustrated in Figure 4.7. In the first triplet, g is aligned with one of the three axes, while in the second triplet, g is oriented in the opposite direction to one of the three axes.
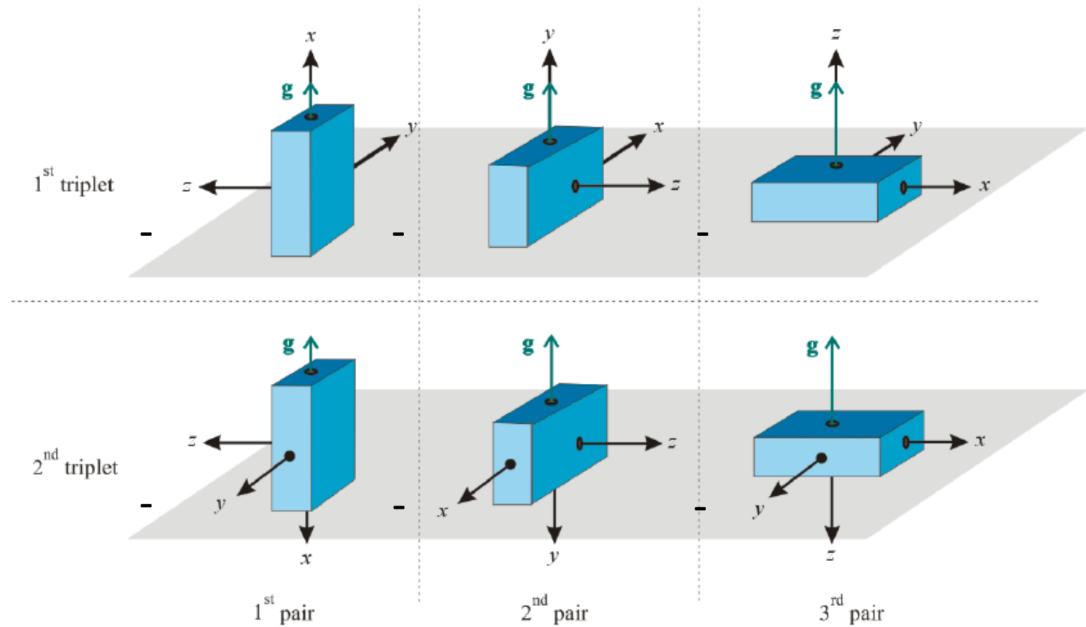
Figure 4.7: Six measurements divided into two triplets with the sensor at rest on a horizontal surface in six different orientations

The acquired measurements will be utilized to estimate C_s and a_0 through the equations proposed by Stancin and Tomazic [63].

After determining C_s and a_0, these parameters are applied to the accelerometer measurements to align them more closely with the ideality condition. The ideality condition is achieved when an accelerometer, placed on a horizontal surface, records the gravity vector along the vertical axis and registers null measurements along the other two horizontal axes. This condition implies that the accelerometer's reference

34

system is perfectly orthogonal, with an axis coincident with the vertical.
The application of C_s transforms the signals from the pre-calibration accelerometer reference system to the post-calibration accelerometer reference system.
The effect of a_0 is to subtract an offset value from the measurements, adjusting the modulus of the post-calibration measurements to approach the ideality condition, where the modulus equals the gravity vector.

Gyroscope calibration

In a similar way, we formulate a calibration model for the gyroscope as follows:

$$\omega = C_s(\omega_s - \omega_0) \tag{4.3}$$

where:

- ω represents the vector of measurements post refinement of the calibration,

- ω_s represents the vector of measurements as read by the gyroscope,

- ω_0 represents the vector of accelerometer offsets,

- C_s represents the matrix of scaling coefficients, which consolidates the effects of the M, C and S matrices.

The influence of temperature is disregarded for simplicity. The calibration's objective is to estimate C_s and ω_0.
Through the four acquisitions shown in Figure 4.8, including:

- A static acquisition,

- A rotation around x,

- A rotation around y,

- A rotation around z,

calibration refinement is to be executed. The gyroscope is situated on a turntable whose axis of rotation aligns with one of the gyroscope's axes, as depicted in Figure 4.9.
For each dynamic acquisition, a known number of complete rotations is performed in a time T. Then, the average ideal velocity of each axis is defined as follows:

$$\omega_i = \frac{\varphi_i}{T}, \ \varphi i = 360° * N_{rotations} \tag{4.4}$$

After determining C_s and ω_0, they are applied to the gyroscope measurements to obtain measurements closer to the ideality condition. The same considerations made for the accelerometer case are applicable in this context.
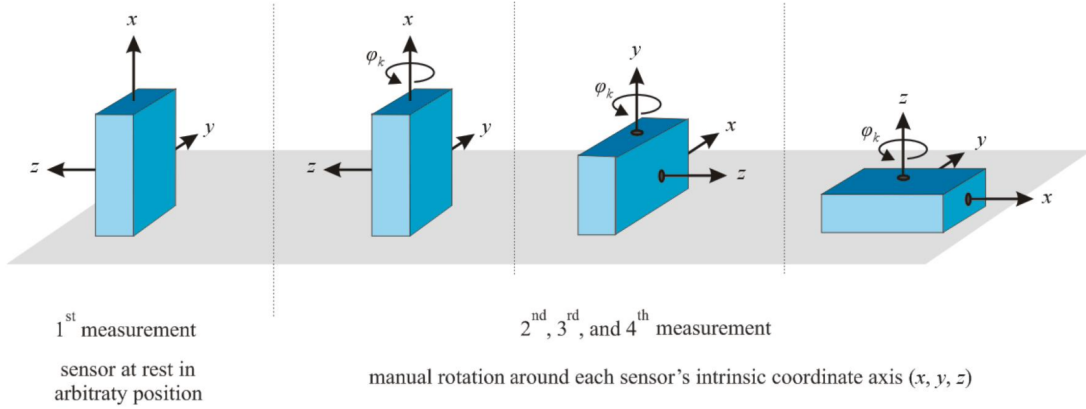
Figure 4.8: Measurements for gyroscope calibration
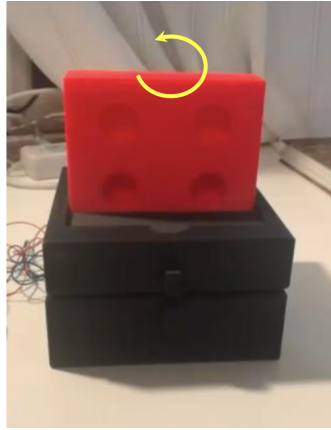
Figure 4.9: Turntable on which the gyroscope is placed during dynamic acquisitions

4.2   Experimental protocol

A validation protocol was followed, involving sensor warm-up to mitigate temperature effects [19], gyroscope bias computation, and marker preparation.

The SP system underwent masking, full calibration, and setting of the laboratory reference system before subject preparation.

The subject was prepared with both optoelectronic markers and IMUs for the walking exercises, as illustrated in Figure 4.10. Static acquisitions allowed for manual labeling of markers, ensuring accurate association with camera-detected points. Post-processing steps involved Nexus software, including gap filling for marker occlusion, dynamic pipeline execution, and ASCII export for data extraction.

The study involved a healthy 22-year-old male subject, and various exercises were performed to analyze straight walking under different conditions:

- Walking at different speeds:

  - Comfortable speed
  - High speed
  - Low speed

- Half-step walking:

  - Right half-step
  - Left half-step

- Toe-walking

- Walking with different step lengths:

  - Short step length
  - Long step length

These exercises were meticulously captured and analyzed using the combined SP and IMU systems, as follows:

1. 10 minutes of warm-up of IMUs,

2. Preliminary acquisition in static condition of one minute of the IMUs to estimate the bias of the gyroscope,

3. Start acquisition with IMU software,

4. Start recording with Nexus,

5. Performance of the first exercise,

6. Stop recording with Vicon,

7. Stop IMUs' acquisition,

8. Repeat the steps 3-7 until reaching at least 3 trials,

9. Repeat the steps 3-8 for each exercise.

37
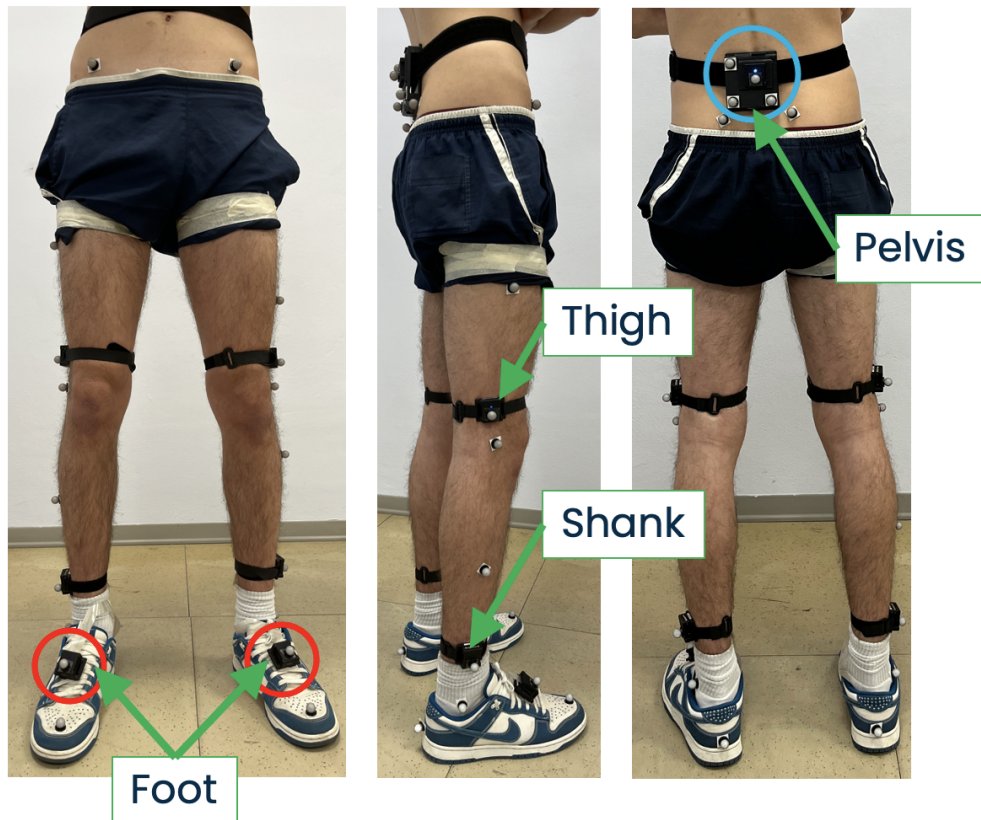
Figure 4.10: Subject's setup with markers and IMUs

For this thesis work, only the "straight walk at comfortable speed" trial was used for the reconstruction of lower limb kinematics.

After completing the acquisition procedure, the data from the INDIP system underwent processing to generate reference outputs. The standardization process resulted in the creation of the Matlab structure "data.mat", encompassing the data acquired by each sensor and adhering to the Mobilise-d project's standards [64]. Specifically:

- The "data.mat" structure contains a field named "TimeMeasure1", which, in turn, comprises multiple fields representing various trials. For each trial, data from different sensors are stored separately, as schematized in Figure 4.11.

- The standardized data adopted the following units of measurement:

  - Accelerations: g
  - Angular velocities: °/s

- Furthermore, data acquired by each triaxial sensor adhered to the convention:

  - The first column represents the anteroposterior component,
  - The second column represents the vertical component,
  - The third column represents the mediolateral component.
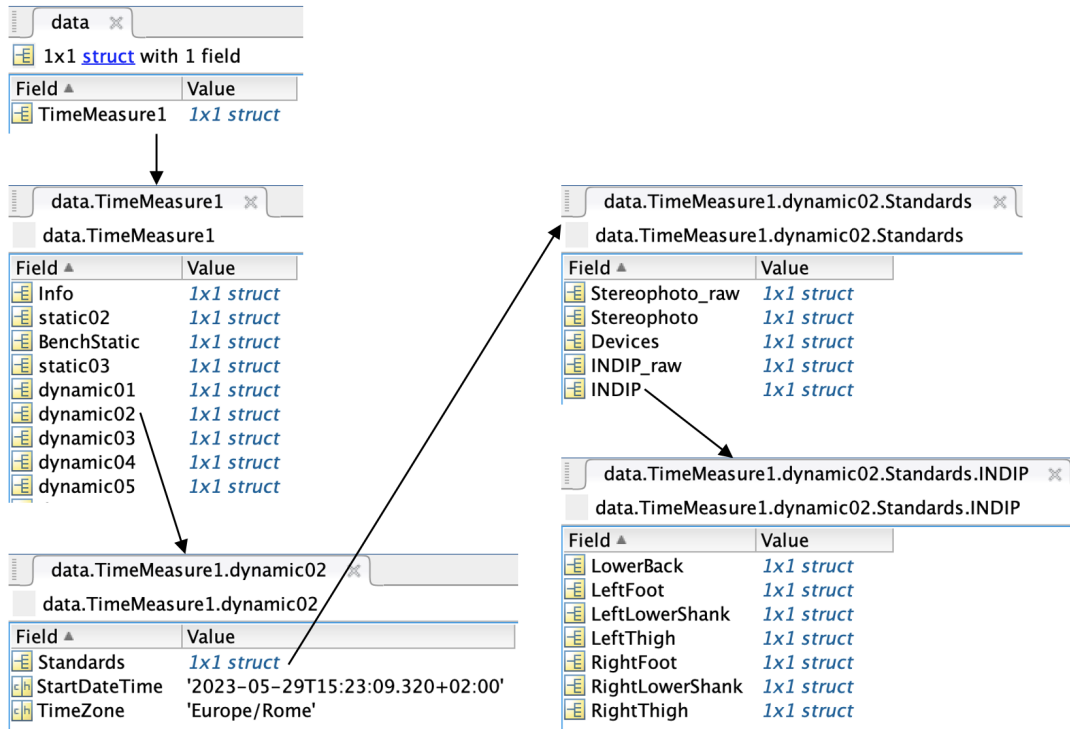
Figure 4.11: Example of how the structure "data.mat" is nested

Chapter 5

Results

Figure 5.1 displays the resulting joint angles for the first cycle, showcasing the flexion-extension angles of the hip, knee, and ankle for each lower limb. Notably, the continuous blue line represents the trends derived from the IMUs, while the dashed red line illustrates the trends from the SP.

These angles play a pivotal role in reconstructing the lower limb kinematics, demonstrated across successive frames in Figure 5.2. In this visualization, the right limb is depicted in blue, while the left limb is depicted in red.

To establish a quantitative comparison between the outcomes derived from the IMUs and those acquired from the SP, RMSE values were computed and are presented in Table 5.1, for each of the three cycles. Additionally, ROM values were calculated for both the angles obtained from the IMUs and those from the SP, along with the differences observed between the two methods. These values are compiled in Table 5.2, for each of the three cycles. For both the RMSE and ROM calculations, the values for the right and left limbs were averaged.

RMSE (deg)	Cycle 1	Cycle 2	Cycle 3
Hip	4.3	3.8	3.8
Knee	6.1	5.3	5.8
Ankle	4.8	4.3	4.2

Table 5.1: RMSE values of the difference between joint angles from the proposed method and from the SP after mean value removal, for each of the three cycles
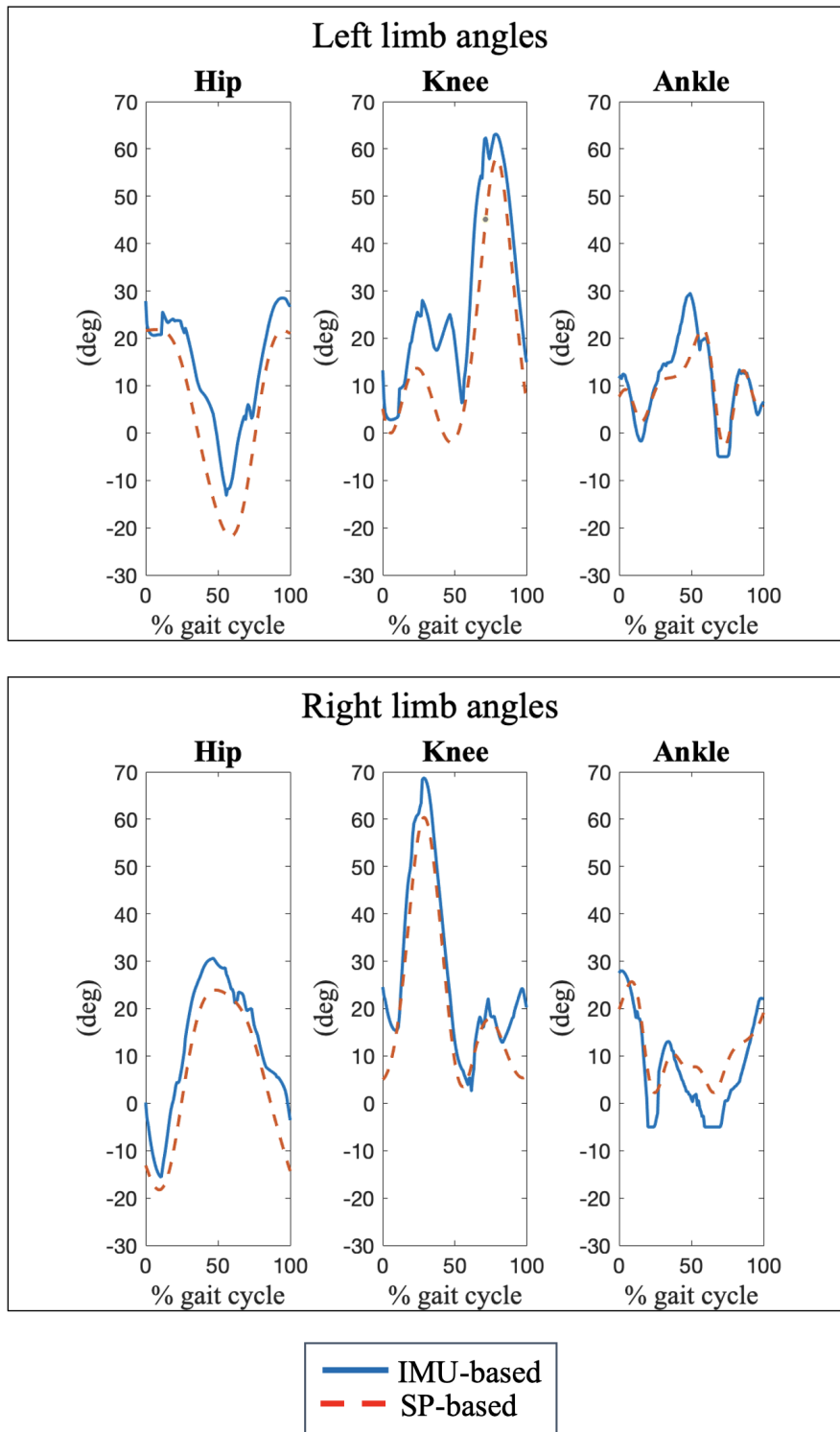
Figure 5.1: Left and right limb angles for hip, knee and ankle from IMUs (in blue) and SP (in red), for the first cycle
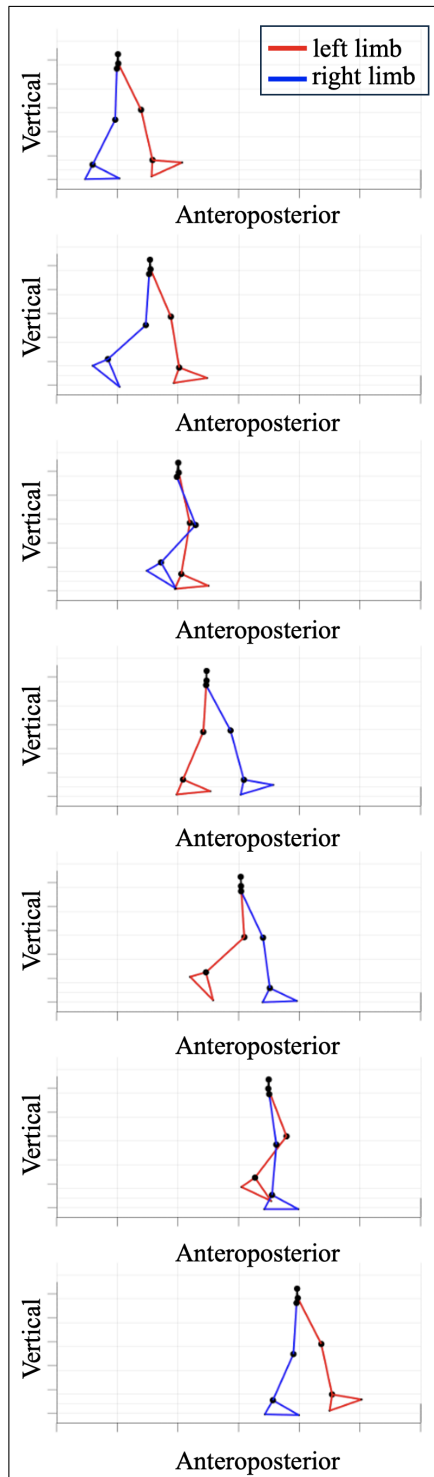
Figure 5.2: Frame sequence of the reconstruction of lower limb kinematics, for the first cycle

Cycle 1			
ROM (deg)	**IMU-based**	**SP-based**	**|IMU-SP|**
Hip	43.9	42.9	1.0
Knee	63.2	58.5	4.7
Ankle	33.7	24.1	9.6
Cycle 2			
ROM (deg)	**IMU-based**	**SP-based**	**|IMU-SP|**
Hip	39.1	42.2	3.1
Knee	55.3	57.5	2.2
Ankle	31.2	24.4	6.8
Cycle 3			
ROM (deg)	**IMU-based**	**SP-based**	**|IMU-SP|**
Hip	41.2	43.3	2.1
Knee	57.0	59.4	2.4
Ankle	32.9	23.9	9.0

Table 5.2: ROM values for hip, knee and ankle from IMUs, SP and the difference between the two methods, for each of the three cycles

Chapter 6

Discussion

6.1   Results on the estimation of joint kinematics

The primary objective of this study was to assess joint kinematics utilizing a simplified setup comprising only three IMUs strategically placed on the feet and pelvis. Specifically, the study aimed to derive angles at the hip, knee, and ankle joints during a selected walking segment. Therefore, three walking segments, each corresponding to a stride, were selected to have three cycles on which to evaluate the results. The selection of walking cycles for analysis was made at random, driven by the observed repeatability of results across different walking cycles. However, a specific criterion was applied to ensure consistency; cycles with initial conditions corresponding to instances of the standing phase, derived from spatial parameters, were considered. This selection was made irrespective of whether these instances pertained to the left or right foot.

A 22-year-old healthy male participant walked in the laboratory along a straight path at a comfortable speed, equipped with the specified three IMUs and markers for the SP system. The data collected from the IMUs were integrated into the optimization framework alongside model-derived data to reconstruct joint kinematics. Subsequently, this reconstruction was compared with the joint kinematics obtained from the SP system.

As depicted in Figure 5.1, the flexion-extension angles at the hip, knee, and ankle joints, derived from the optimization framework, were juxtaposed with those obtained from the SP. The trends exhibited demonstrated the framework's capability to reconstruct joint motion, albeit with noticeable errors. Utilizing these angles, the kinematics of the lower limbs was reconstructed, visualized through a sequence of frames in Figure 5.2, capturing various moments of the gait during the analyzed stride. Similar results were obtained for the other two cycles.

For a quantitative comparison between the trends obtained through optimization

and those obtained through SP, aiming to quantify the errors incurred, the decision was made to calculate the errors between the two methodologies in terms of RMSE for each joint, averaged between the right and left limbs. The selection of the RMSE metric is grounded in its ability to accentuate differences between the two methods by eliminating their mean values. This approach effectively mitigates any inherent offsets arising from the distinct definitions of anatomical reference systems in the two methods, enabling a more meaningful and accurate comparison [58]. The obtained results, summarized in Table 5.1, were then assessed according to the criteria established in McGinley's study [2], indicating that a joint kinematics estimation system is deemed acceptable with RMSE values of less than 5 degrees. Consequently, the errors for the hip and ankle fall within the acceptable range for each of the three cycles, while the error at the knee, recorded at 6.1, 5.3 and 5.8 degrees, respectively, exceeds the acceptable threshold. This can be rationalized by the absence of sensors on the thigh and leg, making it inherently challenging to derive accurate angles at the knee.

Beyond the RMSE assessment, the ROM values were computed for each joint, averaging between the left and right limbs. The computation of the ROM served as a basis for comparing the range of values obtained between the two methods. This analysis is valuable for potential adjustments to the constraints placed on joint angles, aiming to enhance the outcomes derived from the optimization framework. The calculations were performed for both the optimization and SP cases, along with a comparison of the two methods, as presented in Table 5.2. Notably, the analysis reveals, for each of the three cycles, the most significant deviations occurring at the ankle, with a recorded value of 9.6, 6.8 and 9.0 degrees, respectively. This could be attributed to the fact that the ankle angles exhibits peaks that deviate from SP patterns, particularly saturating during foot extension, as depicted in Figure 5.1. In contrast, the deviations for the hip and knee are comparatively smaller.

In computing RMSE and ROM, a decision was made to average the values obtained for the right and left limbs. This choice was motivated by the fact that, depending on the segment of the path used for reconstructing lower limb kinematics, the optimization's initial conditions vary. Consequently, the framework may encounter more challenges for either limb based on its initial position.

It is crucial to highlight that the lower limb kinematics within the implemented framework adheres to the ISB standards. More precisely, the biomechanical model constructed enables the correlation of body segment orientations with the generalized coordinates of the multi-segmental chain, maintaining compliance with ISB guidelines.

The ultimate aspiration involves employing this promising sensor configuration in conjunction with the developed model to reconstruct lower limb kinematics in real-world scenarios, encompassing various types of gait and accommodating different subject conditions. In fact, the implemented framework offers the concurrent

integration of constraints, encompassing both joint motion limitations and specific attributes characterizing the analyzed experiment. Consequently, this capability enables the examination of various walking scenarios. By preemptively identifying the type of exercise under consideration, the framework allows for the introduction and subsequent modification of pertinent constraints. This dynamic adjustment process aims to enhance the precision of results derived from the optimization framework.

As previously emphasized in the Section 3.5, the position of the pelvis and feet obtained from the SP instead of the IMUs was utilized at this stage of the study, representing a crucial aspect for future development. Implementing this step is essential for assessing the variability of errors in the reconstruction of joint kinematics. It is noteworthy to emphasize that positions derived from IMUs inherently harbor errors, especially in the case of foot positions obtained from disparate and independent systems. The extent of mismatch between these distinct systems directly correlates with the magnitude of errors manifested in position measurements. This recognition underscores the necessity of leveraging SP-derived data at this stage of the work in refining the accuracy of joint kinematics reconstruction.

Moreover, when considering foot positions obtained from the IMUs, the accurate identification of standing phase instants becomes crucial. Incorrect identification of these instants can propagate errors, since they play a key role in assuming zero mean value of acceleration, which is removed after subtraction of gravity, in establishing initial conditions for integration, and in assuming zero velocity, which is critical for reinitiating orientation. In the latter case, if the assumption is not met, accelerometer measurements encompass not only gravity but also a component associated with the actual acceleration of the body.

Another influential factor contributing to errors is the accuracy of anthropometric lengths input into the model. Incorrect anthropometric lengths introduce a discrepancy in position measurements, as these lengths delineate a spectrum of possible positions used within the optimization process.

6.2   Future Developments

Concerning the pelvis position, a prospective advancement involves substituting values obtained from the SP with those derived from IMUs. This could be achieved by modeling the pelvis trajectory during the analyzed step cycle using an inverse pendulum, as detailed in [65]. The referenced paper leverages the bipodal support and balance phases of gait. In the balance phase, the foot emulates an inverted pendulum, where the ankle joint serves as the support, and the tibia acts as the pendulum, coordinating movement with the knee joint. Throughout the walking cycle, the contact area of the foot sole with the ground can be regarded as the

joint of the reverse pendulum, while the pelvic region represents the free end of the pendulum, illustrated in Figure 6.1.
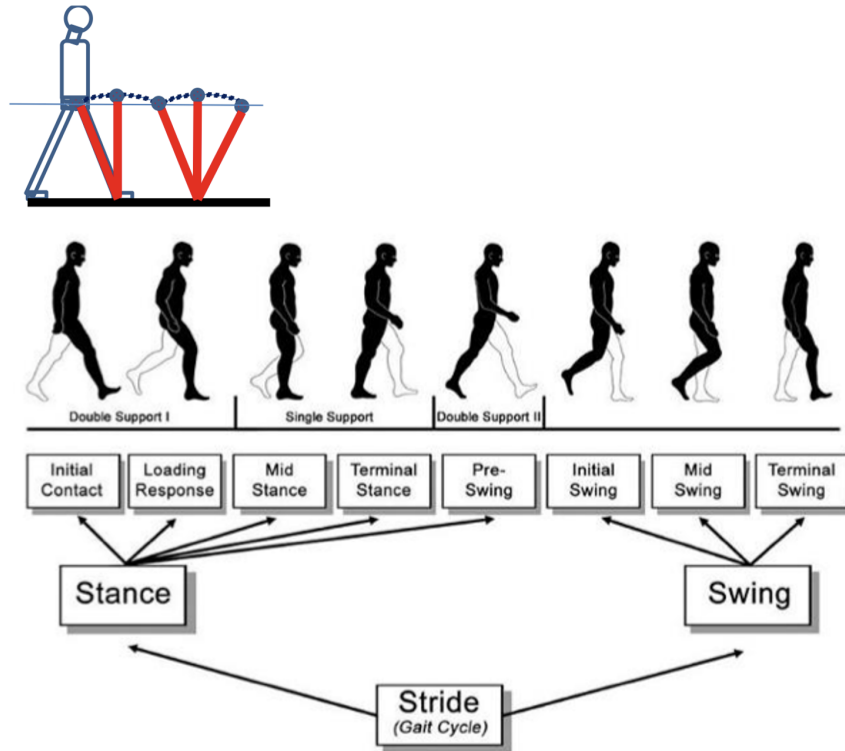
Figure 6.1: Model of the walking cycle with the inverted pendulum [65]

Subsequently, efforts can be directed towards refining the framework to minimize the errors further. Nevertheless, the current work established the feasibility of the initial objective, providing a foundation for future advancements.

As a concluding note, it is noteworthy to mention that the present optimization framework requires 0.38 seconds for a single iteration. Therefore, as another avenue for future development, efforts can be directed towards reducing this computational time. Such optimization would be particularly beneficial for constructing real-time applications of the framework.

Chapter 7

Conclusions

In the field of human movement analysis, the precise quantification of kinematic intricacies during real-life gait assumes paramount importance. This pursuit has the potential to significantly influence diagnostic methodologies for motor disorders and inform the design and evaluation of rehabilitation interventions. The dynamic aspects of human gait, particularly walking speed, have attained recognition as a vital sign alongside traditional indicators. Despite the precision offered by quantitative instrumented gait analysis, its widespread clinical integration encounters substantial logistical challenges. The emergent technologies of wearables and sensor fusion techniques present promising alternatives, offering viable solutions for efficient gait monitoring in naturalistic environments.

This thesis addressed the impracticality of full-body sensor networks in real-world scenarios by proposing a minimal configuration comprising three strategically IMUs on the feet and pelvis. The objective was to estimate lower limb kinematics by leveraging spatio-temporal parameters and IMU-derived orientations, notwithstanding inherent errors associated with such measurements.

The study employed an optimization framework based on the DH convention, introducing constraints to mitigate information gaps and errors. Through experimental validation comparing results with a SP system, RMSE values were derived. While errors for hip and ankle joints fell within acceptable thresholds (less than 5 degrees), those for the knee joint exceeded the established criterion.

The proposed framework adheres to ISB standards, facilitating its potential application in real-world scenarios and suggesting avenues for further refinement. Future endeavors include the enhancement of foot and pelvis position measurements and optimization of computational efficiency. Despite existing limitations, this work established the viability of the proposed IMU-based system, laying the groundwork for advancing clinical gait analysis methodologies.

Bibliography

[1] Salis F. et al. «A multi-sensor wearable system for the assessment of diseased gait in real-world conditions». In: *Frontiers in Bioengineering and Biotechnology* 1 (Apr. 2023) (cit. on pp. i, 3, 18).

[2] McGinley J.L., Baker R., Wolfe R., and Morris M.E. «The reliability of three-dimensional kinematic gait measurements: a systematic review». In: *Gait Posture* 29.3 (Apr. 2009), pp. 360–369 (cit. on pp. ii, 45).

[3] Fritz S. and Lusardi M. «White paper: walking speed: the sixth vital sign». In: *Journal of Geriatric Physical Therapy* 32.2 (2009), pp. 46–49 (cit. on p. 1).

[4] Hulleck A.A., Menoth Mohan D., Abdallah N., El Rich M., and Khalaf K. «Present and future of gait assessment in clinical practice: Towards the application of novel trends and technologies». In: *Frontiers in Medical Technology* 4 (Dec. 2022) (cit. on p. 1).

[5] Trojanello D. «Assessment of gait spatio-temporal parameters in neurological disorders using wearable inertial sensors». PhD thesis. Bologna: Alma Mater Studiorum, 2015 (cit. on p. 2).

[6] Mazzà C. et al. «Technical validation of real-world monitoring of gait: a multicentric observational study». In: *BMJ Open* 11.12 (Dec. 2021) (cit. on p. 2).

[7] Dejnabadi H., Jolles B.M., and Aminian K. «A new approach to accu- rate measurement of uniaxial joint angles based on a combination of accelerometers and gyroscopes». In: *IEEE Transactions on Biomedical Engineering* 52.8 (Aug. 2005), pp. 1478–1484 (cit. on p. 5).

[8] Kobashi S., Kawano K., Tsumori Y., Yoshiya S., and Hata Y. «Wearable joint kinematic monitoring system using inertial and magnetic sensors». In: *2009 IEEE Workshop on Robotic Intelligence in Informationally Structured Space.* Nashville, TN, USA, Mar. 2009, pp. 25–29 (cit. on p. 5).

[9] Zhu R. and Zhou Z. «A real-time articulated human motion tracking using tri-axis inertial/magnetic sensors package». In: *IEEE Transactions on Neural systems and rehabilitation engineering* 12.2 (June 2004), pp. 295–302 (cit. on pp. 5, 6).

[10] Cereatti A., Trojaniello D., and Della Croce U. «Accurately measuring human movement using magneto-inertial sensors: techniques and challenges». In: *2015 IEEE International Symposium on Inertial Sensors and Systems (ISISS) Proceedings*. Hapuna Beach, HI, USA, Mar. 2015, pp. 1–4 (cit. on pp. 6, 7).

[11] Bergamini E., Ligorio G., Summa A., Vannozzi G., and Cappozzo A. adn Sabatini A.M. «Estimating orientation using magnetic and inertial sensors and different sensor fusion approaches: accuracy assessment in manual and locomotion tasks». In: *Sensors (Basel)* 14.10 (Oct. 2014), pp. 18625–18649 (cit. on pp. 6, 9).

[12] Madgwick S. «An efficient orientation filter for inertial and inertial / magnetic sensor arrays». In: University of Bristol (UK), 2010 (cit. on p. 6).

[13] Aydemir G.A and Saranli A. «Characterization and calibration of MEMS inertial sensors for state and parameter estimation applications». In: *Measurement* 45.5 (June 2012), pp. 1210–1225 (cit. on pp. 6, 7).

[14] Unsal D. and Demirbas K. «Estimation of deterministic and stochastic IMU error parameters». In: *Proceedings of the 2012 IEEE/ION Position, Location and Navigation Symposium*. Myrtle Beach, SC, USA, Apr. 2012, pp. 862–868 (cit. on pp. 6, 7).

[15] Nez A., Fradet L., Laguillaumie P., Monnet T., and Lacouture P. «Comparison of calibration methods for accelerometers used in human motion analysis». In: *Medical Engineering and Physics* 38.11 (Nov. 2016), pp. 1289–1299 (cit. on p. 6).

[16] Aslan G. and Saranli A. «Characterization and calibration of MEMS inertial measurement units». In: *2008 16th European Signal Processing Conference*. Lausanne, Switzerland, Aug. 2008, pp. 1–5 (cit. on p. 7).

[17] Kirkko-Jaakkola M., Collin J., and Takala J. «Bias Prediction for MEMS Gyroscopes». In: *IEEE Sensors Journal* 12.6 (June 2012), pp. 2157–2163 (cit. on p. 7).

[18] Ferraris F., Grimaldi U., and Parvis M. «Procedure for effortless in-field calibration of three-axial rate gyro and accelerometers». In: *Sensors and Materials* 7.5 (1995), pp. 311–330 (cit. on p. 7).

[19]   Caruso M., Sabatini A.M., Laidig D., Seel T., Knaflitz M., Della Croce U., and Cereatti A. «Analysis of the Accuracy of Ten Algorithms for Orientation Estimation Using Inertial and Magnetic Sensing under Optimal Conditions: One Size Does Not Fit All». In: *Sensors (Basel)* 21.7 (Apr. 2021), p. 2543 (cit. on pp. 7, 36).

[20]   Gulmammadov F. «Analysis, modeling and compensation of bias drift in MEMS inertial sensors». In: *2009 4th International Conference on Recent Advances in Space Technologies.* Istanbul, Turkey, June 2009, pp. 591–596 (cit. on p. 7).

[21]   Hiller T., Pentek Z., Liewald J.T., Buhmann A., and Roth H. «Origins and Mechanisms of Bias Instability Noise in a Three-Axis Mode-Matched MEMS Gyroscope». In: *Journal of Microelectromechanical Systems* 28.4 (Aug. 2019), pp. 586–596 (cit. on p. 7).

[22]   Walther A., Le Blanc C., Delorme N., Deimerly Y., Anciant R., and Willemin J. «Bias Contributions in a MEMS Tuning Fork Gyroscope». In: *Journal of Microelectromechanical Systems* 22.2 (Apr. 2013), pp. 303–308 (cit. on p. 7).

[23]   Madgwick S.O., Harrison A.J., and Vaidyanathan A. «Estimation of IMU and MARG orientation using a gradient descent algorithm». In: *2011 IEEE International Conference on Rehabilitation Robotics.* ETH Zurich Science City, Switzerland, June 2011 (cit. on pp. 8, 19, 21).

[24]   Lebel K., Boissy P., Hamel M., and Duval C. «Inertial measures of motion for clinical biomechanics: comparative assessment of accuracy under controlled conditions - effect of velocity». In: *PLoS One* 8.11 (Nov. 2013) (cit. on p. 9).

[25]   Lebel K., Boissy P., Hamel M., and Duval C. «Inertial measures of motion for clinical biomechanics: comparative assessment of accuracy under controlled conditions - changes in accuracy over time». In: *PLoS One* 10.3 (Mar. 2015) (cit. on p. 9).

[26]   Ludwig S.A. and Burnham K.D. «Comparison of Euler Estimate using Extended Kalman Filter, Madgwick and Mahony on Quadcopter Flight Data». In: *2018 International Conference on Unmanned Aircraft Systems (ICUAS).* Dallas, TX, USA, June 2018, pp. 1236–1241 (cit. on p. 9).

[27]   Nazarahari M. and Rouhani H. «40 years of sensor fusion for orientation tracking via magnetic and inertial measurement units: Methods, lessons learned, and future challenges». In: *Information Fusion* 68 (Apr. 2021), pp. 67–84 (cit. on p. 9).

[28]   Ricci L., Taffoni F., and Formica D. «On the Orientation Error of IMU: Investigating Static and Dynamic Accuracy Targeting Human Motion». In: *PLoS One* 11.9 (Sept. 2016) (cit. on p. 9).

[29] Weber D., Gühmann C., and Seel T. «Neural Networks Versus Conventional Filters for Inertial-Sensor-based Attitude Estimation». In: *2020 IEEE 23rd International Conference on Information Fusion (FUSION)*. Rustenburg, South Africa, July 2020, pp. 1–8 (cit. on p. 9).

[30] Young A.D. «Comparison of Orientation Filter Algorithms for Realtime Wireless Inertial Posture Tracking». In: *2009 Sixth International Workshop on Wearable and Implantable Body Sensor Networks*. Berkeley, CA, USA, June 2009, pp. 59–64 (cit. on p. 9).

[31] Cavallo A., Cirillo A., Cirillo P., De Maria G., Falco P., Natale C., and Pirozzi S. «Experimental Comparison of Sensor Fusion Algorithms for Attitude Estimation». In: *IFAC Proceedings Volumes* 47.3 (2014), pp. 7585–7591 (cit. on p. 9).

[32] Caruso M. «Methods and good practice guidelines for human joint kinematics estimation through magnetic and inertial wearable sensors». PhD thesis. Torino: Plitecnico di Torino, 2022 (cit. on p. 9).

[33] Olivares A., Górriz J.M., Ramírez J., and Olivares G. «Using frequency analysis to improve the precision of human body posture algorithms based on Kalman filters». In: *Computers in Biology and Medicine* 72 (May 2016), pp. 229–38 (cit. on p. 9).

[34] Bonato P. «Wearable sensors/systems and their impact on biomedical engineering». In: *IEEE Engineering in Medicine and Biology Magazine* 22.3 (May 2003), pp. 18–20 (cit. on p. 9).

[35] Seel T., Raisch J., and Schauer T. «IMU-based joint angle measurement for gait analysis». In: *Sensors (Basel)* 14.4 (Apr. 2014), pp. 6891–6909 (cit. on p. 9).

[36] Wu G. et al. «ISB recommendation on definitions of joint coordinate system of various joints for the reporting of human joint motion–part I: ankle, hip, and spine». In: *Journal of Biomechanics* 35.4 (Apr. 2002), pp. 543–548 (cit. on pp. 9, 10, 16).

[37] Wu G. et al. «ISB recommendation on definitions of joint coordinate systems of various joints for the reporting of human joint motion–Part II: shoulder, elbow, wrist and hand». In: *Journal of Biomechanics* 38.5 (May 2005), pp. 981–992 (cit. on pp. 9, 10).

[38] Cereatti A., Della Croce U., and Sabatini A.M. «Three-Dimensional Human Kinematic Estimation Using Magneto-Inertial Measurement Units». In: *Handbook of Human Motion* (Apr. 2017), pp. 1–24 (cit. on p. 9).

[39] Siciliano B., Sciavicco L., Villani L., and Oriolo G. *Robotics - Modelling, Planning and Control.* Springer London, 2009 (cit. on pp. 14, 15).

[40] Panich S. «Design and Simulation of Leg-Exoskeleton Suit for Rehabilitation». In: *Global Journal of Medical Research* 12.3 (May 2012) (cit. on p. 15).

[41] Chen Y.L., Yang I.J., Fu L.C., Lai J.S., Liang H.W., and Lu L. «IMU-Based Estimation of Lower Limb Motion Trajectory With Graph Convolution Network». In: *IEEE Sensors Journal* 21.21 (Nov. 2021), pp. 24549–24557 (cit. on p. 15).

[42] Caruso M., Gastaldi L., Pastorelli S., Cereatti A., and Digo E. «An ISB-consistent Denavit-Hartenberg model of the human upper limb for joint kinematics optimization: validation on synthetic and robot data during a typical rehabilitation gesture». In: *2022 44th Annual International Conference of the IEEE Engineering in Medicine Biology Society (EMBC)*. Glasgow, Scotland, United Kingdom, 2022, pp. 1805–1808 (cit. on p. 16).

[43] Lencioni T., Carpinella I., Rabuffetti M., Marzegan A., and Ferrari M. «Human kinematic, kinetic and EMG data during different walking and stair ascending and descending tasks». In: *Scientific Data* 6.1 (Dec. 2019), p. 309 (cit. on p. 18).

[44] Valenti R.G., Dryanovski I., and Xiao J. «Keeping a Good Attitude: A Quaternion-Based Orientation Filter for IMUs and MARGs». In: *Sensors (Basel)* 15.8 (Aug. 2015), pp. 19302–19330 (cit. on p. 20).

[45] Rossanigo R., Caruso M., Salis F., Bertuletti S., Della Croce U., and Cereatti A. «An Optimal Procedure for Stride Length Estimation Using Foot-Mounted Magneto-Inertial Measurement Units». In: *2021 IEEE International Symposium on Medical Measurements and Applications (MeMeA)*. Lausanne, Switzerland, June 2021, pp. 1–6 (cit. on p. 21).

[46] Mariani B., Hoskovec C., Rochat S., Büla C., Penders J., and Aminian K. «3D gait assessment in young and elderly subjects using foot-worn inertial sensors». In: *Journal of Biomechanics* 43.15 (Nov. 2010), pp. 2999–3006 (cit. on p. 21).

[47] Skog I., Händel P., Nilsson J.O., and Rantakokko J. «Zero-velocity detection — an algorithm evaluation». In: *IEEE Transactions on Biomedical Engineering* 57.11 (Nov. 2010) (cit. on p. 21).

[48] Zok M., Mazzà C., and Della Croce U. «Total body centre of mass displacement estimated using ground reactions during transitory motor tasks: application to step ascent». In: *Medical Engineering and Physics* 26.9 (Nov. 2004), pp. 791–798 (cit. on pp. 21, 22).

[49] Salarian A., Russmann H., Vingerhoets F.J., Dehollain C., Blanc Y., Burkhard P.R., and Aminian K. «Gait assessment in Parkinson's disease: toward an ambulatory system for long-term monitoring». In: *IEEE Transactions on Biomedical Engineering* 51.8 (Aug. 2004), pp. 1434–1443 (cit. on p. 21).

[50] Trojaniello D., Cereatti A., Pelosin E., Avanzino L., Mirelman A., Hausdorff J.M., and Della Croce U. «Estimation of step-by-step spatio-temporal parameters of normal and impaired gait using shank-mounted magneto-inertial sensors: application to elderly, hemiparetic, parkinsonian and choreic gait». In: *Journal of NueroEngineering and Rehabilitation* 11.1 (Nov. 2014), p. 152 (cit. on p. 21).

[51] Peruzzi A., Della Croce U., and Cereatti A. «Estimation of stride length in level walking using an inertial measurement unit attached to the foot: a validation of the zero velocity assumption during stance». In: *Journal of Biomechanics* 44.10 (July 2011), pp. 1991–1994 (cit. on p. 21).

[52] Xie L., Yang P., Wang C., Gu T., Duan G., Lu X., and Lu S. «GaitTracker: 3D Skeletal Tracking for Gait Analysis Based on Inertial Measurement Units». In: *ACM Transactions on Sensor Networks* 18.2 (Mar. 2022), pp. 1–27 (cit. on p. 22).

[53] Wikipedia contributors. *Sequential quadratic programming — Wikipedia, The Free Encyclopedia.* [Online; accessed 24-October-2023]. 2009. URL: https://en.wikipedia.org/wiki/Sequential_quadratic_programming (cit. on pp. 23, 24).

[54] Nocedal J. and Wright S.J. *Numerical Optimization, Second Edition.* Springer, 2006 (cit. on p. 23).

[55] Spellucci P. «A new technique for inconsistent QP problems in the SQP method». In: *Journal of Mathematical Methods of Operations Research* 47.3 (Oct. 1998), pp. 355–400 (cit. on p. 25).

[56] Tone K. «Revisions of constraint approximations in the successive QP method for nonlinear programming problems». In: *Journal of Mathematical Programming* 26.2 (June 1983), pp. 144–152 (cit. on p. 25).

[57] Byrd R.H., Hribar M.E., and Nocedal J. «An Interior Point Algorithm for Large-Scale Nonlinear Programming». In: *SIAM Journal on Optimization* 9.4 (1999), pp. 877–900 (cit. on p. 25).

[58] Picerno P., Cereatti A., and Cappozzo A. «Joint kinematics estimate using wearable inertial and magnetic sensing modules». In: *Gait Posture* 28.4 (Nov. 2008), pp. 588–595 (cit. on pp. 27, 45).

[59] Vicon. *Plug-in Gait Reference Guide.* Mar. 2022 (cit. on pp. 28, 30).

[60] Salis F., Bertuletti S., Caruso M., Della Croce U., Mazzà C., and Cereatti A. «Multi-sensor integration and data fusion for enhancing gait assessment in and out of the laboratory». In: *Gait Posture* 74 (Sept. 2019), p. 34 (cit. on p. 30).

[61] Salis F., Bertuletti S., Scott K., Caruso M., Bonci T., Buckley E., Della Croce U., Mazzà C., and Cereatti A. «A wearable multi-sensor system for real world gait analysis». In: *2021 43rd Annual International Conference of the IEEE Engineering in Medicine Biology Society (EMBC)*. Nov. 2021, pp. 7020–7023 (cit. on pp. 30, 31).

[62] Bertuletti S., Cereatti A., Comotti D., Caldara M., and Della Croce U. «Static and Dynamic Accuracy of an Innovative Miniaturized Wearable Platform for Short Range Distance Measurements for Human Movement Applications». In: *Sensors (Basel)* 17.7 (June 2017), p. 1492 (cit. on p. 31).

[63] Stančin S. and Tomažič S. «Time- and computation-efficient calibration of MEMS 3D accelerometers and gyroscopes». In: *Sensors (Basel)* 14.8 (Aug. 2014), pp. 14885–14915 (cit. on pp. 33, 34).

[64] Palmerini L. et al. «Mobility recorded by wearable devices and gold standards: the Mobilise-D procedure for data standardization». In: *Scientific Data* 10.1 (Jan. 2023), p. 38 (cit. on p. 38).

[65] Tătaru A.I. and Baritz M.I. «Development of biomechanical gait analysis based on inverted pendulum theory». In: *IOP Conference Series: Materials Science and Engineering* 1256.1 (Oct. 2022) (cit. on pp. 46, 47).